Supporting Online Material

Timing Errors

Systematic and correctable timing errors were introduced by software bugs in various versions of the Quanterra data logger. Such timing errors remained undocumented at various networks (e.g., Geofon) but were generally fixed by software upgrades before the turn of the millennium. This problem was significant for the LH channels, and all our data have been appropriately corrected. Many stations also have periods of erratic timing which are likely due to loss of an external timing standard. Such data have been removed from further analysis.

Technical Aspects of the Inversion

Because the short-period P waves originate from the nucleation point on the fault surface, whereas long-period waves average over the rupture process, we use independent hypocentral corrections for the 5,938 events for which we have long-period travel times, and the 86,499 events for which we have short-period times.

The velocity structure is represented through linear interpolation between a set of flexibly spaced nodes that form a three-dimensional, tetrahedral, Delaunay mesh [1–3]. The node spacing increases with the expected resolving length of our data, and ranges from about 200 km in the upper mantle to about 600 km in the lower mantle. The grid consists of 19,279 nodes. Together with the hypocentral corrections we have a total of 389,027 unknowns, which we seek to resolve with 1,584,764 observations. The influence of data errors upon the tomographic image is kept under control by regularization: the source parameters are damped to give a posteriori shifts comparable to their a priori error estimates; the Euclidean norm of the velocity inversion is only slightly damped; the inversion is mostly regularized by implementing a three-dimensional Laplacian smoothing [4].

To avoid domination of the solution by the much larger short-period data set, we weight the least-squares system such that the reduced chi-squared χ^2_{red} (χ^2 divided by the number of data) is about equal for each data set separately. The preferred model satisfies the short-period data with $\chi^2_{\mathrm{red}} = 1.1$, whereas the long period data are fitted with $\chi^2_{\mathrm{red}} = 1.2$. In test inversions of the data sets separately, we noted a tendency for the long-period data to produce higher anomalies by as much as 50%; the two independently inverted models correlate well, with a depth-dependent correlation coefficient around 0.6. The χ^2_{red} values obtained for the combined inversion show that the amplitude difference is not due to a pronounced difference in the internal consistency of the delay times. This difference may indicate that even the ISC data are subject to wavefront healing, or that we overestimate the errors in the ISC data set, or that there are as yet unknown biases in the data. It is noteworthy, however, that the plumes that are visible in the low-frequency inversion are also recognizable (though often weaker) in the high-frequency inversion, indicating that it is the full combination of all improvements (culling of the highest quality short-period data and remeasurement of the long-period data, in addition to the implementation of finite-frequency sensitivity kernels and an irregular model parameterization) that have enabled us to image deep mantle plumes. We combine the long-period and short-

period travel times in a single inversion to exploit the difference in sensitivities of the two data sets.

The Resolution of Plumes

To test the resolution, we generated 'synthetic' data sets for Earth models with cylindrical Gaussian anomalies $\delta v_{\rm P}/v_{\rm P} = (\delta v_{\rm P}/v_{\rm P})_{\rm cent} \exp(-r^2/w^2)$ with radii $w = 100$, 200, 300 and 400 km; centered at a large number of observed plumes, and extending to depths of 650, 1000, ..., 2800 km (as in Figs. 2, 3 and S1). Synthetic traveltime residuals were computed using finite-frequency sensitivity kernels for the long-period data and using standard ray theory for the short-period data. The highest velocity perturbation $(\delta v_{\rm P}/v_{\rm P})_{\rm cent}$ in the center of the cylinder is defined by following the pattern for temperature derivative $dv_{\rm P}/dT$ of P-wave velocity in the mantle as a function of depth given by Karato [5, Fig. 1]. Assuming a temperature contrast $\Delta T = 300^\circ$ K at the center of the plume, the maximum velocity perturbation is -1% below 1000 km depth, -1.2% between 600 and 1000 km depth, and -2.4% above 600 km depth (Fig. S1). After adding noise with the same assigned standard deviations as in the actual data, these synthetic data were inverted using the same regularization, and the images were inspected for agreement with the input image used to generate them. We consider a plume to be 'resolved' if the recovered synthetic image has a contrast $|\delta v_{\rm P}/v_{\rm P}| > 0.3\%$, i.e., well above the level of ubiquitous noisy fluctuations in the actual images. This threshold corresponds to a temperature contrast of the order of 100 K in the lower mantle [5]. In addition to testing the influence of ray coverage, the test also reveals when our interpolation scheme affects the image.

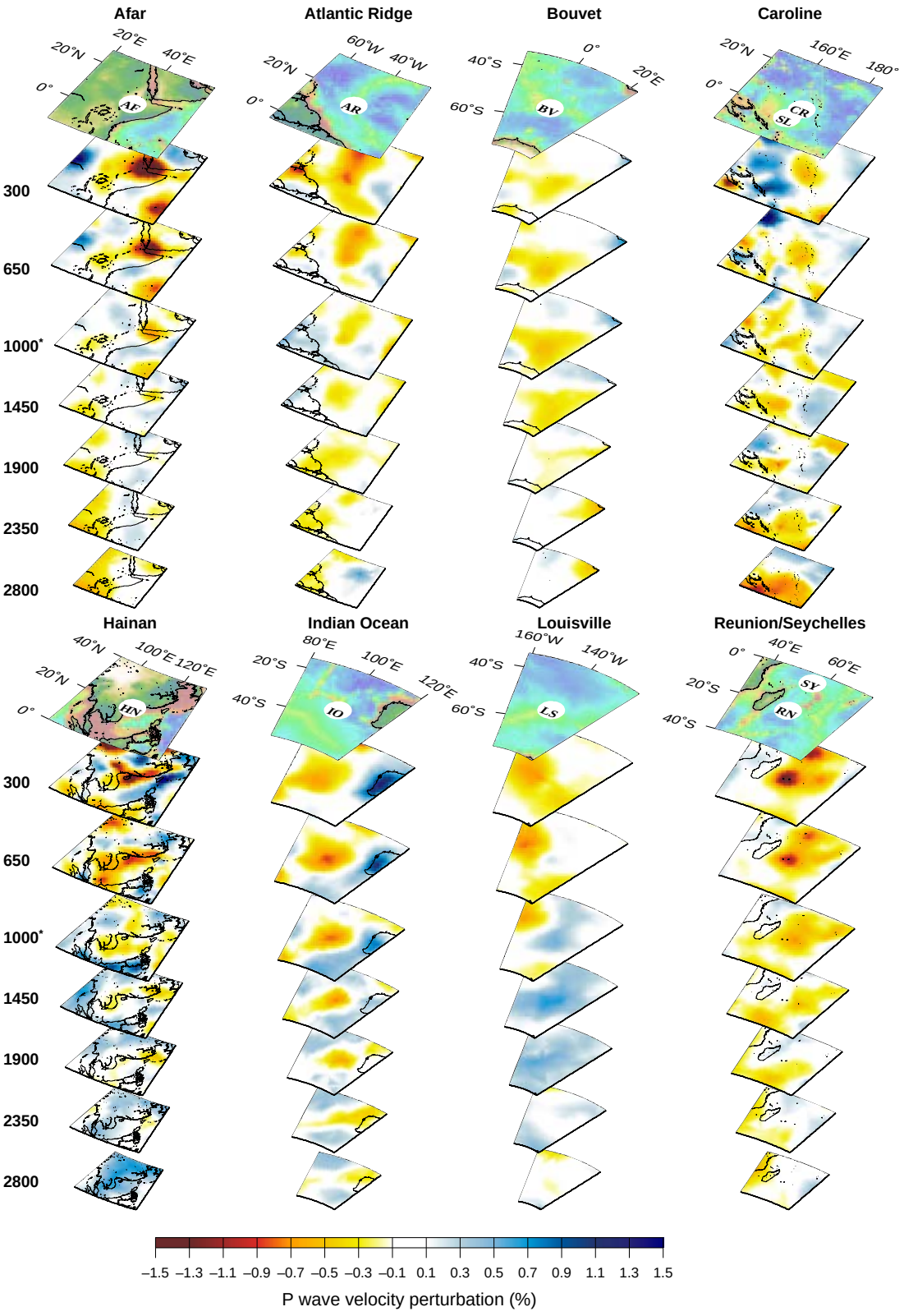

Figure S1: Three-dimensional views of the plumes that seem to originate in the mid-mantle. Plotting format, including change in depth scaling at 1000 km is identical to that of Figs. 2 and 3.

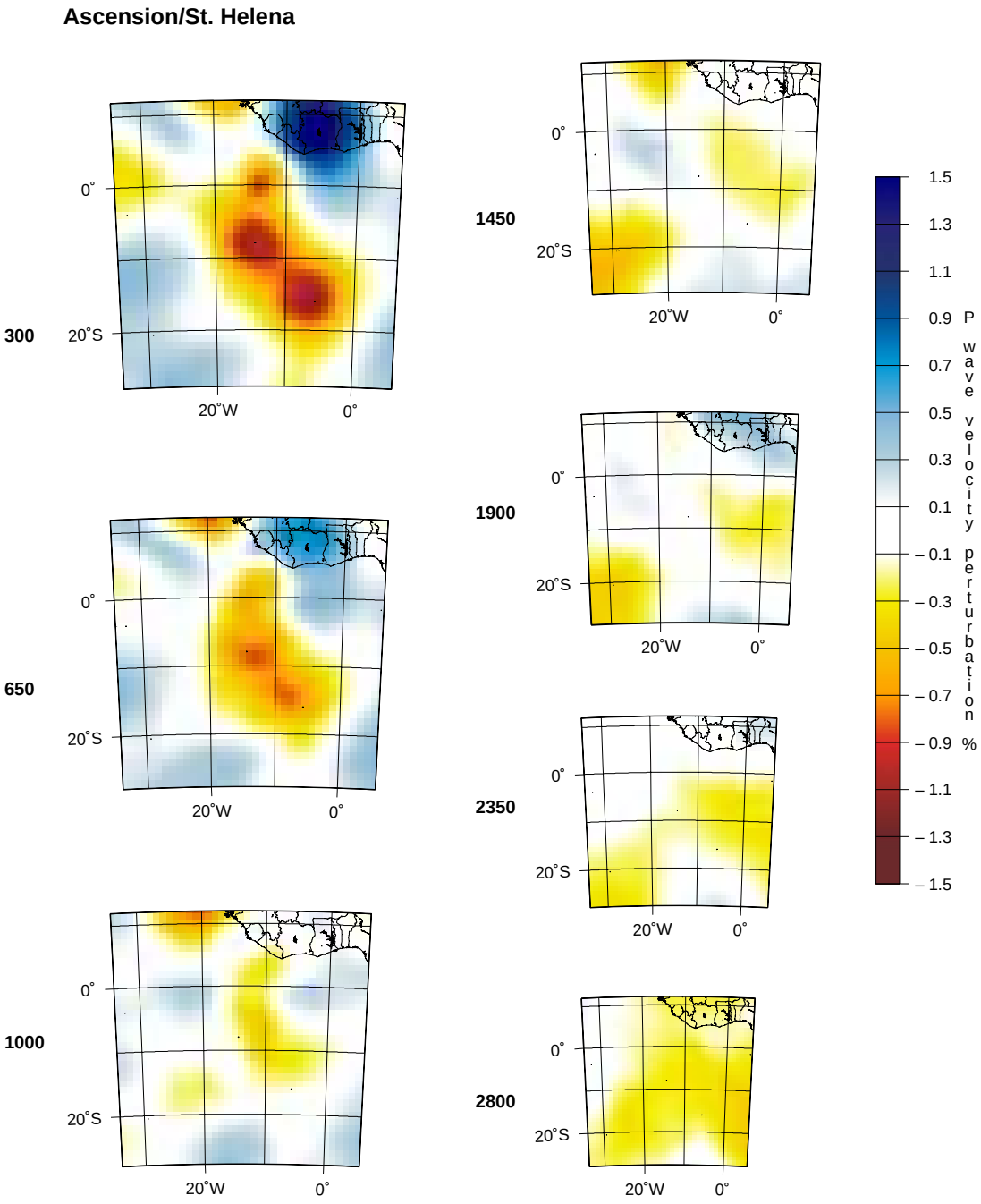

Figure S2: Sections of the velocity model at different depths (300, 650, 1000, 1450, 1900, 2350 and 2800 km) beneath Ascension and St. Helena. The sections are the same as in Fig. 2 but projected on a flat plane to help the visualization of the velocity anomaly.

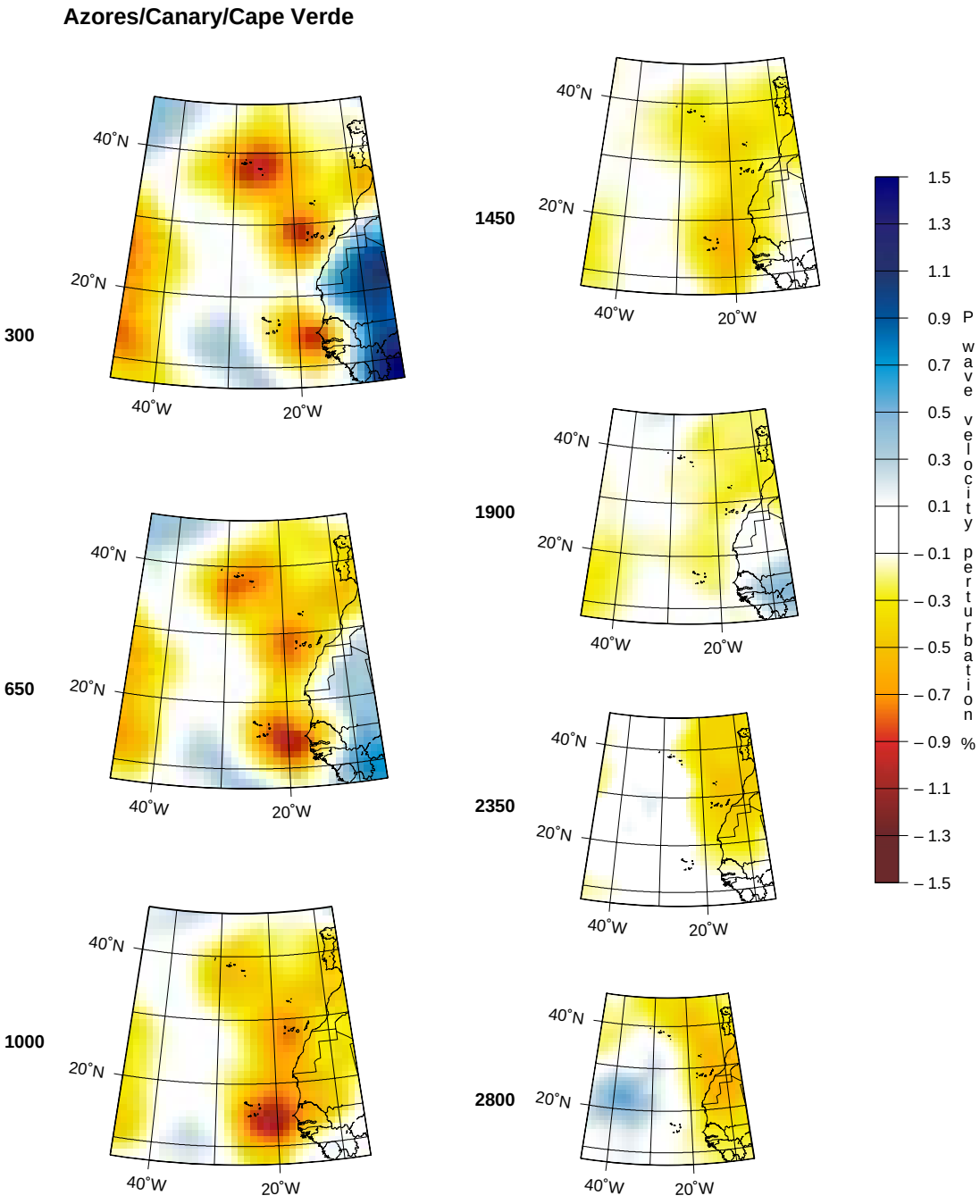

Figure S3: Sections of the velocity model beneath Azores, Canary and Cape Verde (Fig. 2). Plotting format is the same as in Fig. S2.

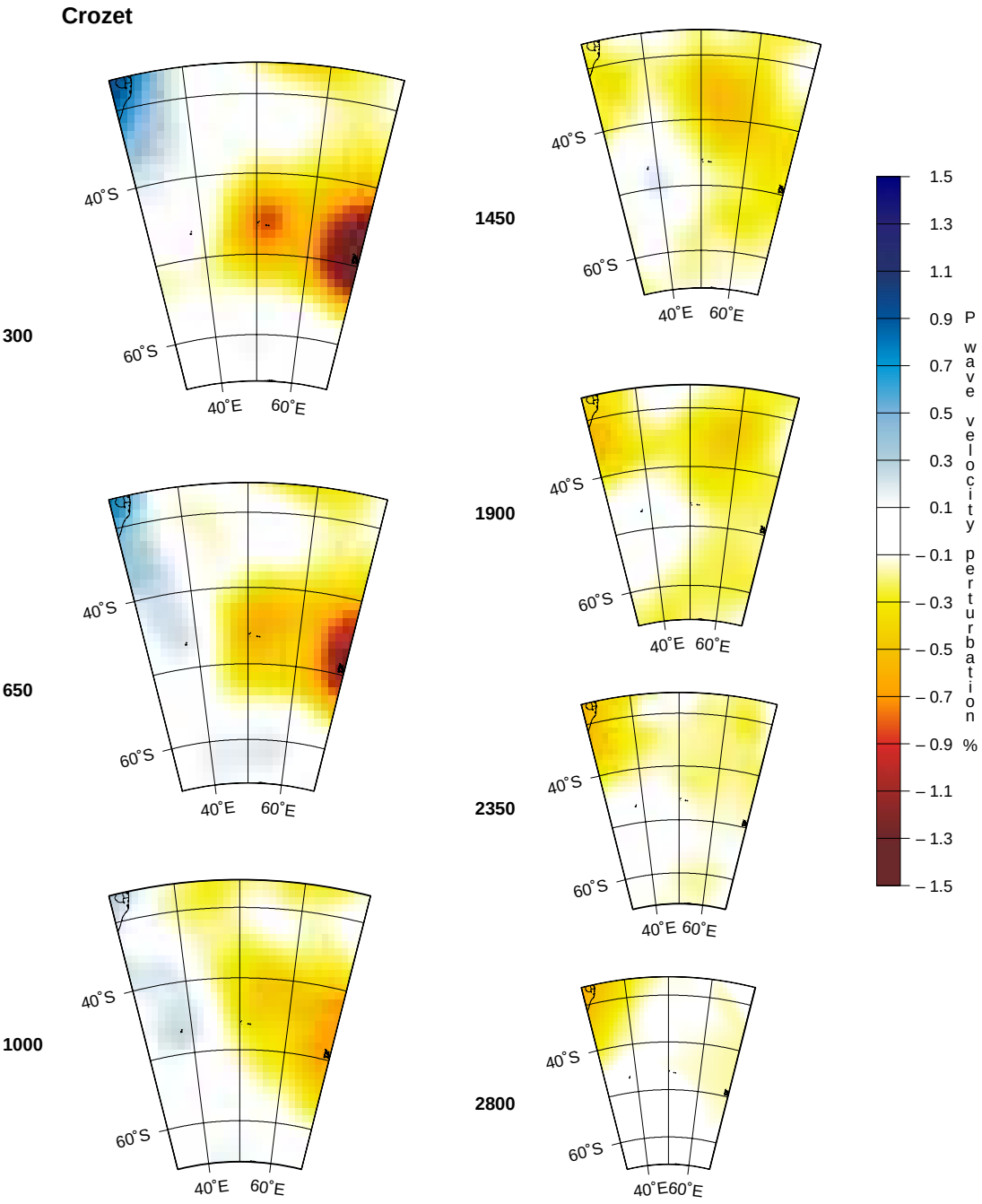

Figure S4: Sections of the velocity model beneath Crozet (Fig. 2). Plotting format is the same as in Fig. S2.

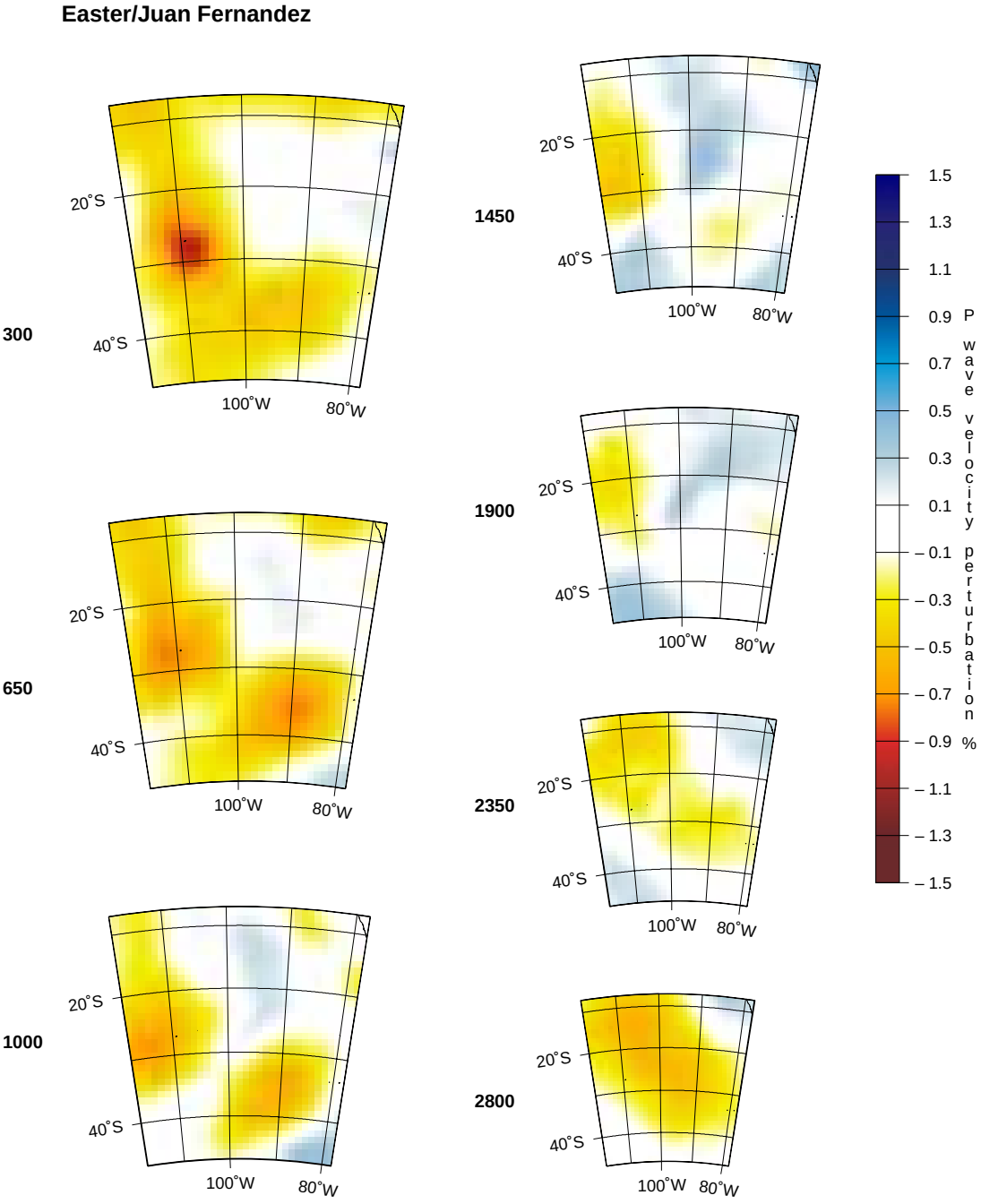

Figure S5: Sections of the velocity model beneath Easter and Juan Fernandez (Fig. 2). Plotting format is the same as in Fig. S2.

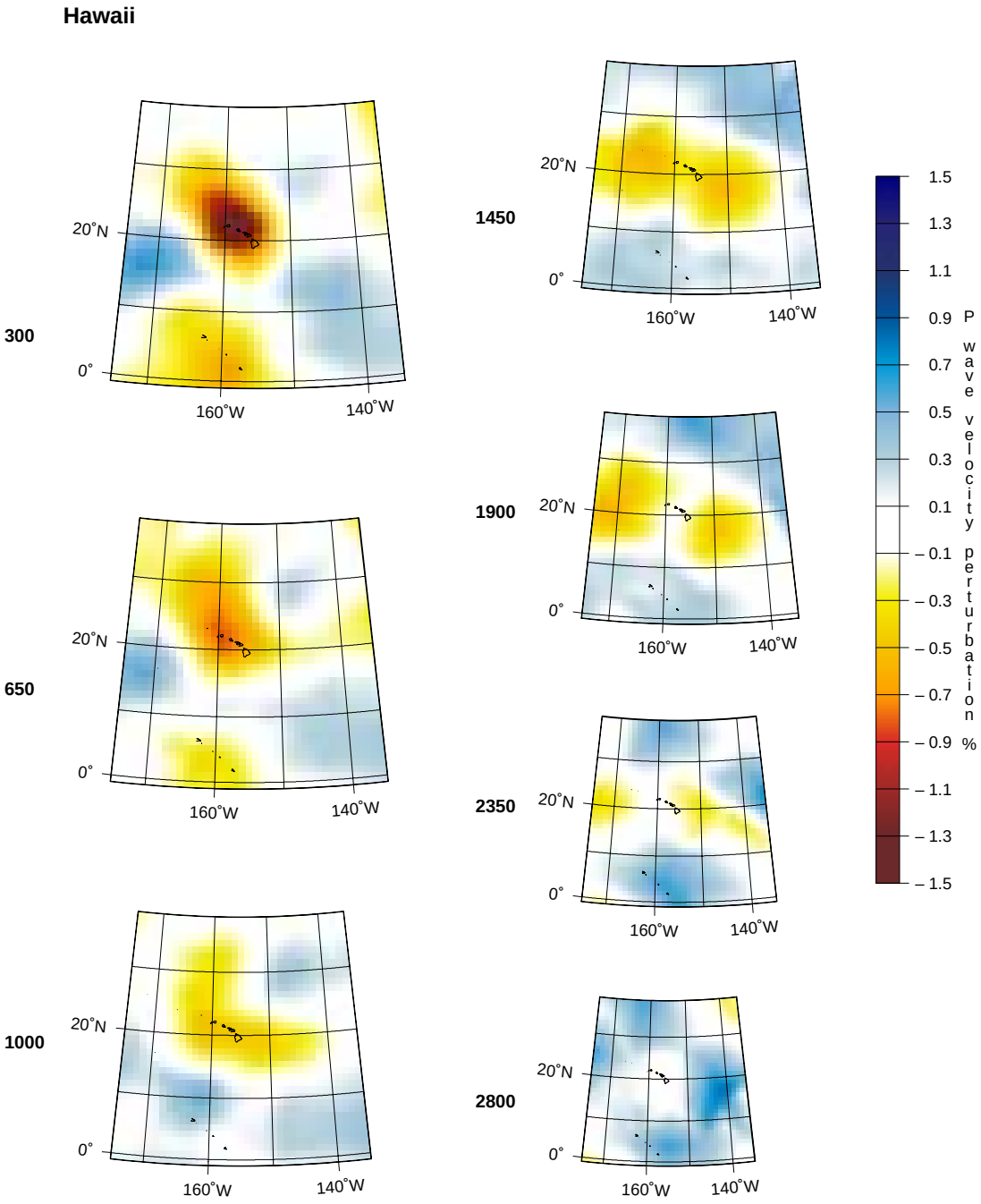

Figure S6: Sections of the velocity model beneath Hawaii (Fig. 2). Plotting format is the same as in Fig. S2.

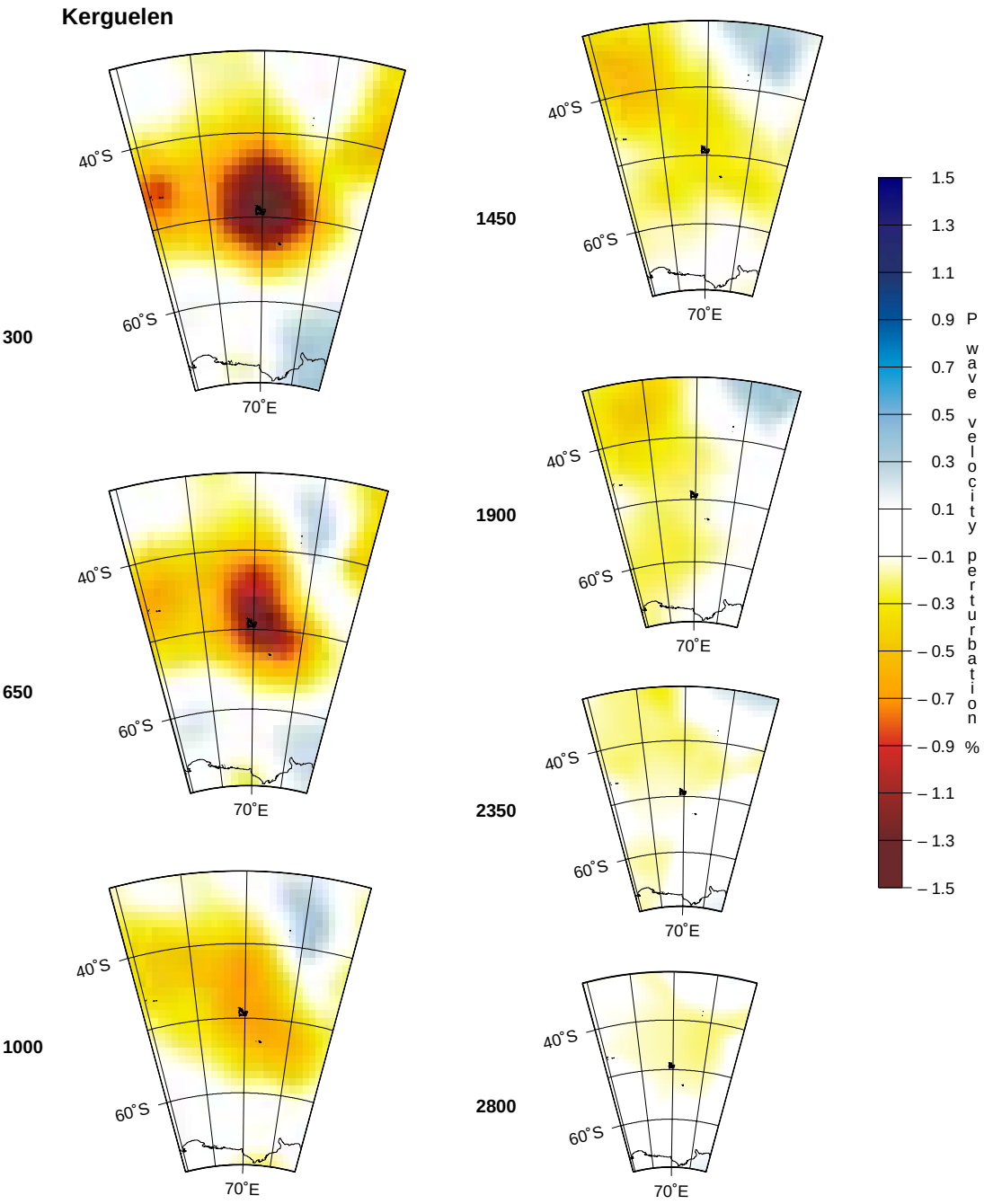

Figure S7: Sections of the velocity model beneath Kerguelen (Fig. 2). Plotting format is the same as in Fig. S2.

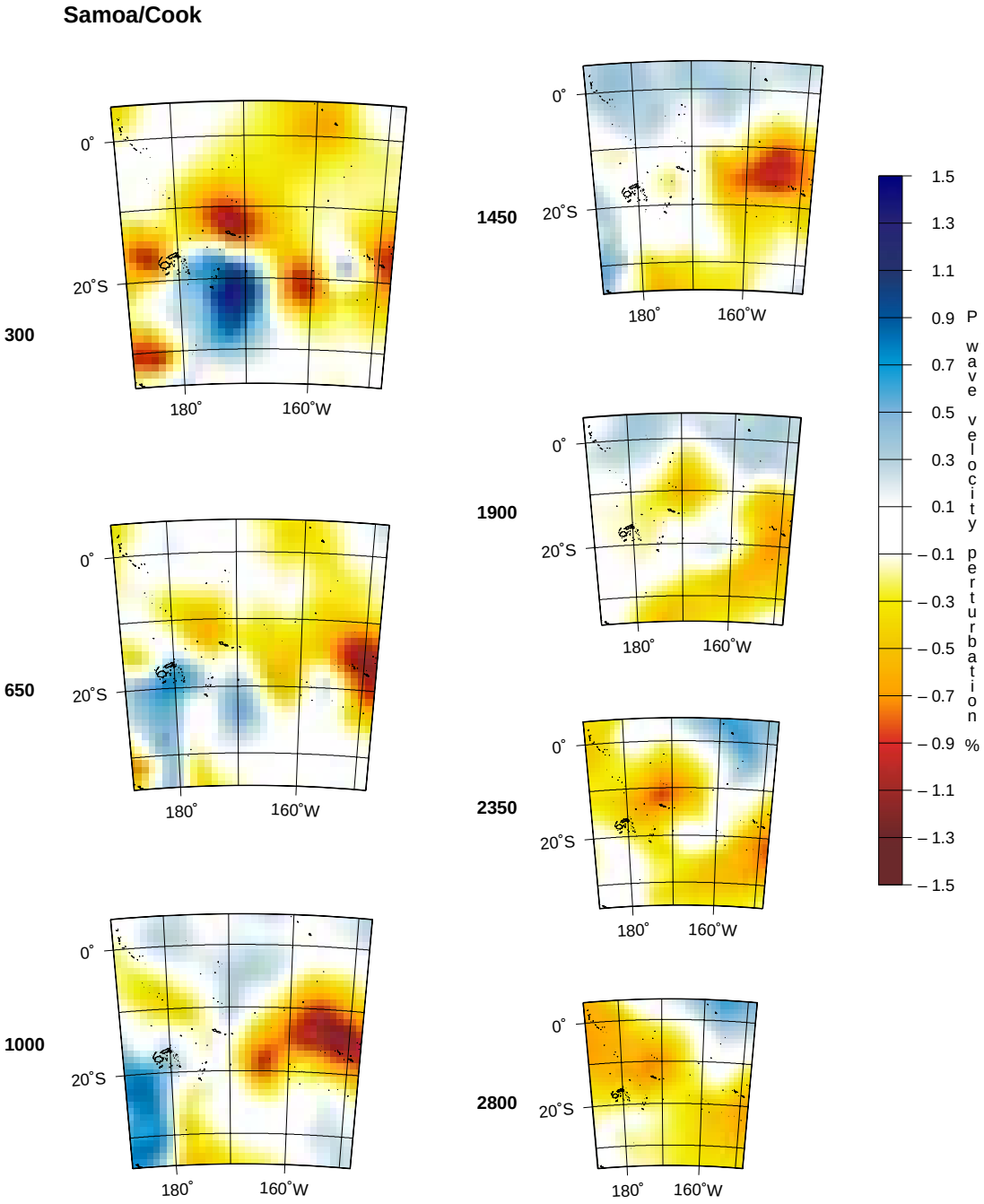

Figure S8: Sections of the velocity model beneath Samoa and Cook Islands (Fig. 2). Plotting format is the same as in Fig. S2.

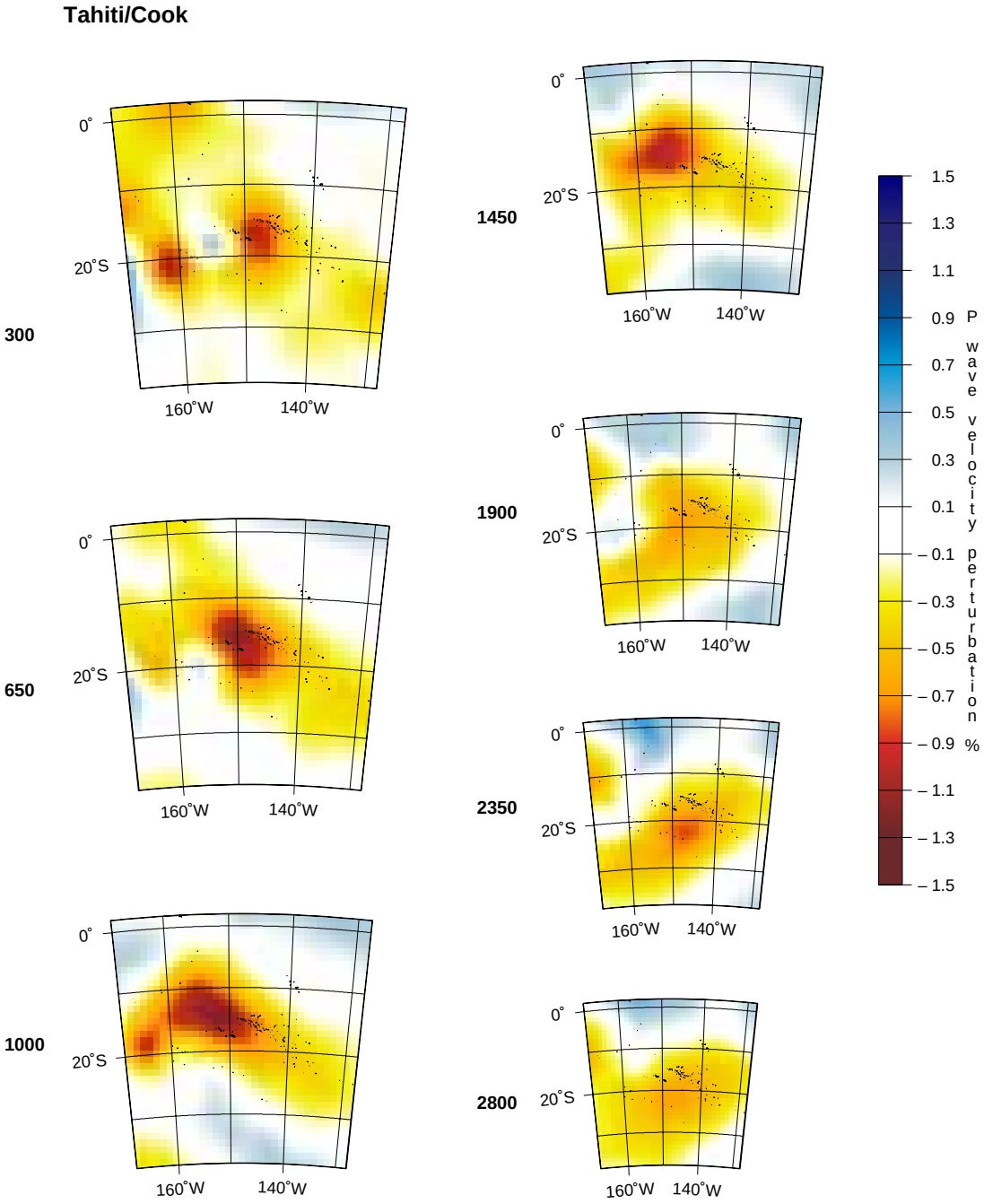

Figure S9: Sections of the velocity model beneath Tahiti and Cook Islands (Fig. 2). Plotting format is the same as in Fig. S2.

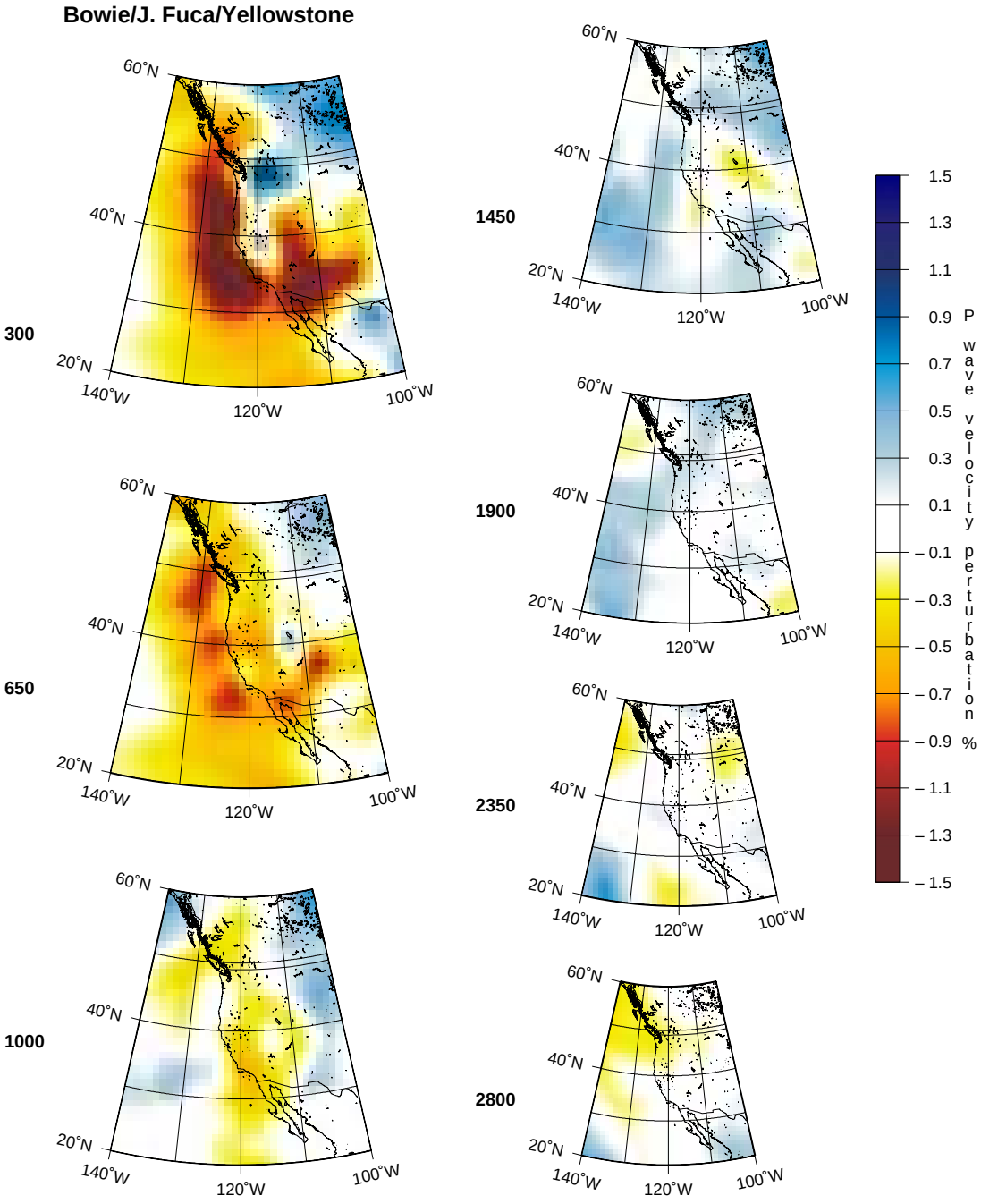

Figure S10: Sections of the velocity model beneath Bowie, Juan de Fuca and Yellowstone (Fig. 3). Plotting format is the same as in Fig. S2.

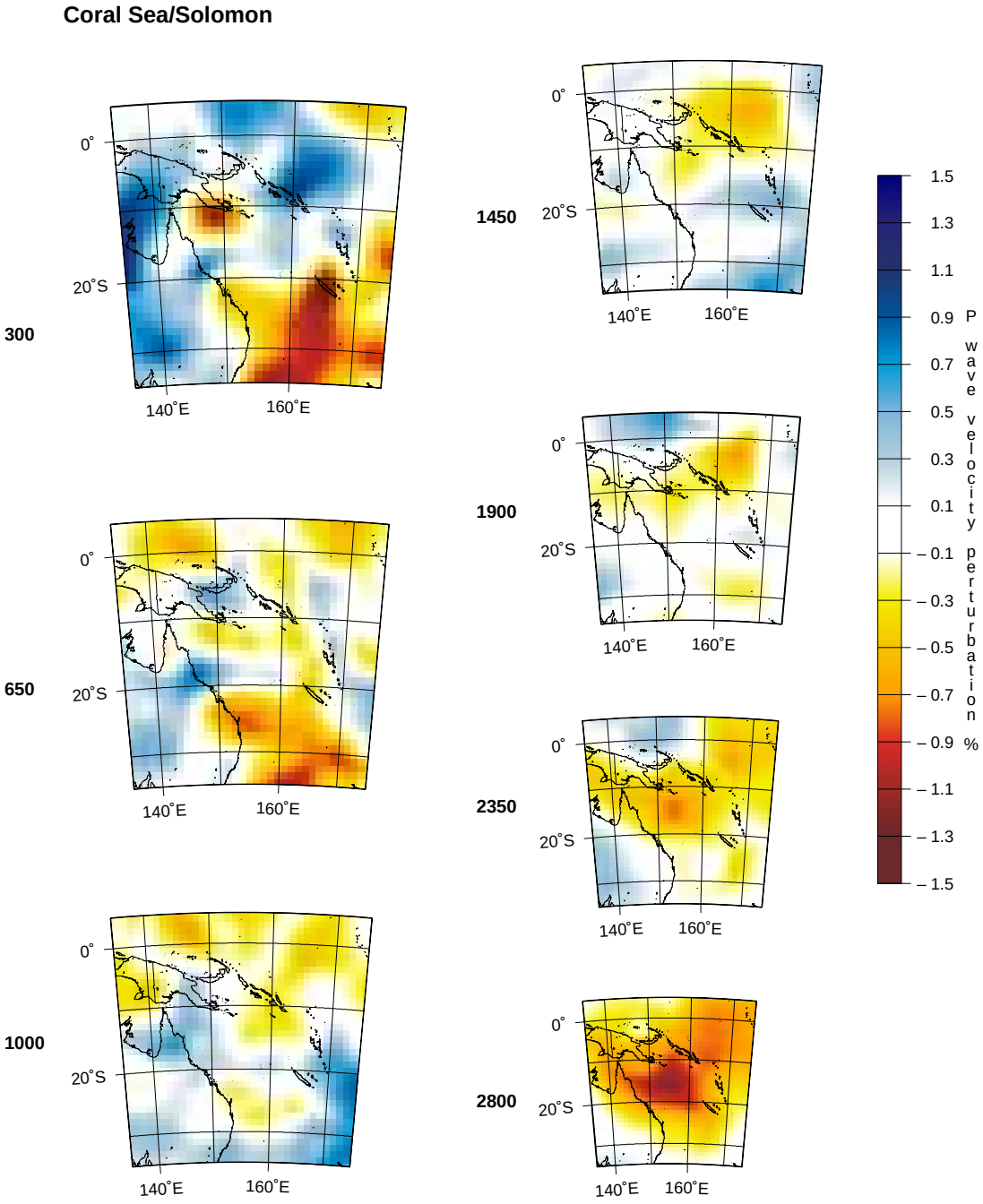

Figure S11: Sections of the velocity model beneath Coral Sea and Solomon (Fig. 3). Plotting format is the same as in Fig. S2.

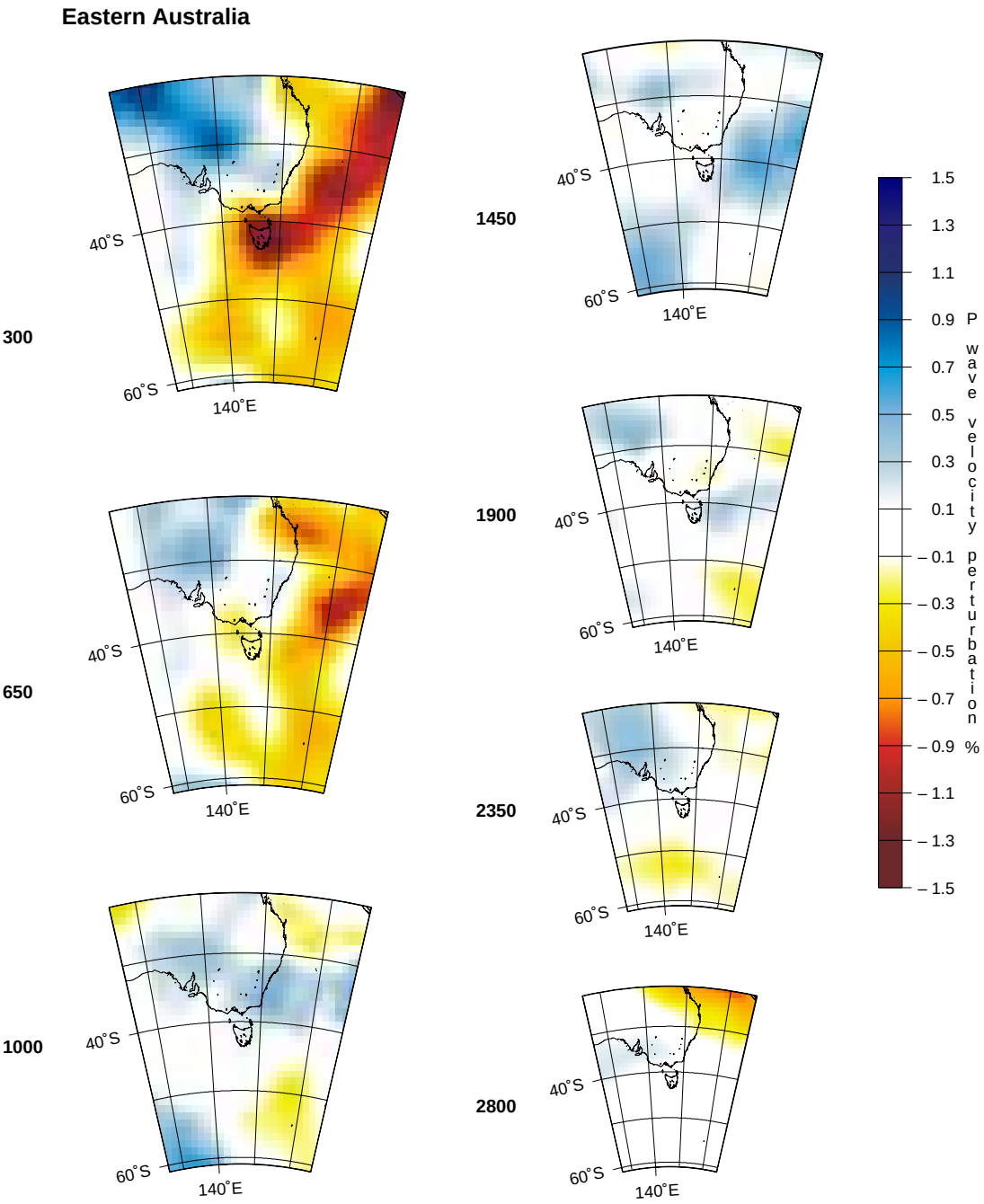

Figure S12: Sections of the velocity model beneath Eastern Australia (Fig. 3). Plotting format is the same as in Fig. S2.

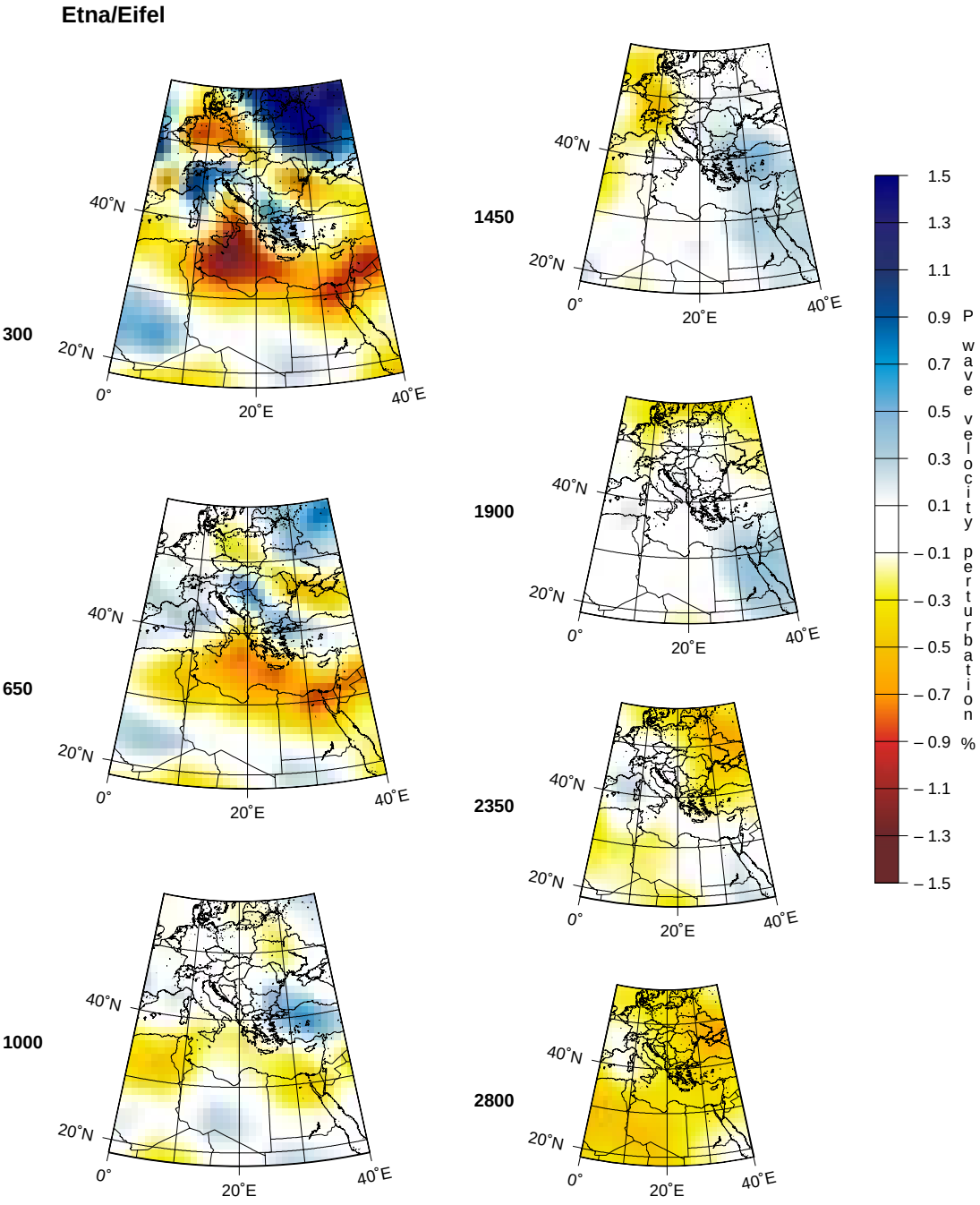

Figure S13: Sections of the velocity model beneath Etna and Eifel (Fig. 3). Plotting format is the same as in Fig. S2.

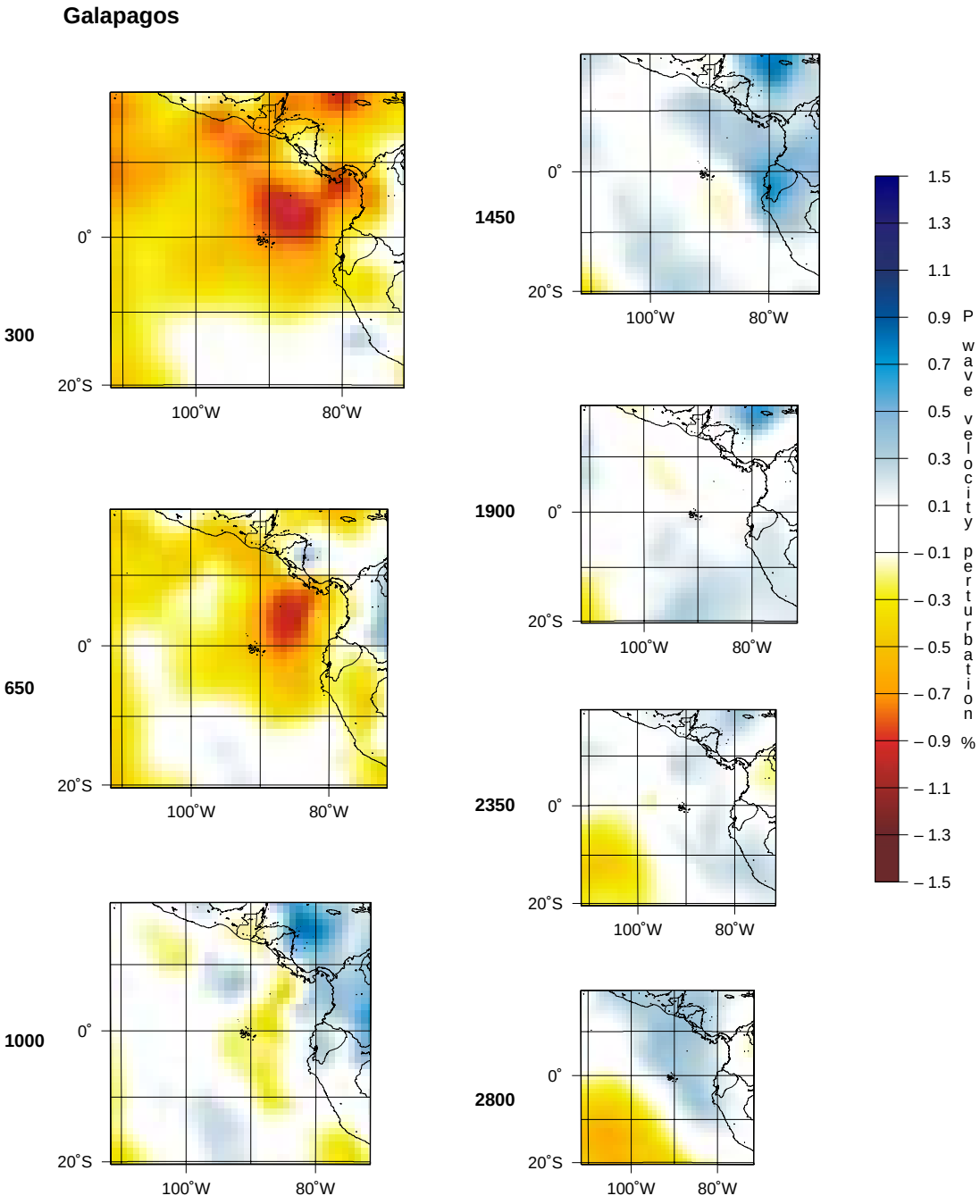

Figure S14: Sections of the velocity model beneath Galapagos (Fig. 3). Plotting format is the same as in Fig. S2.

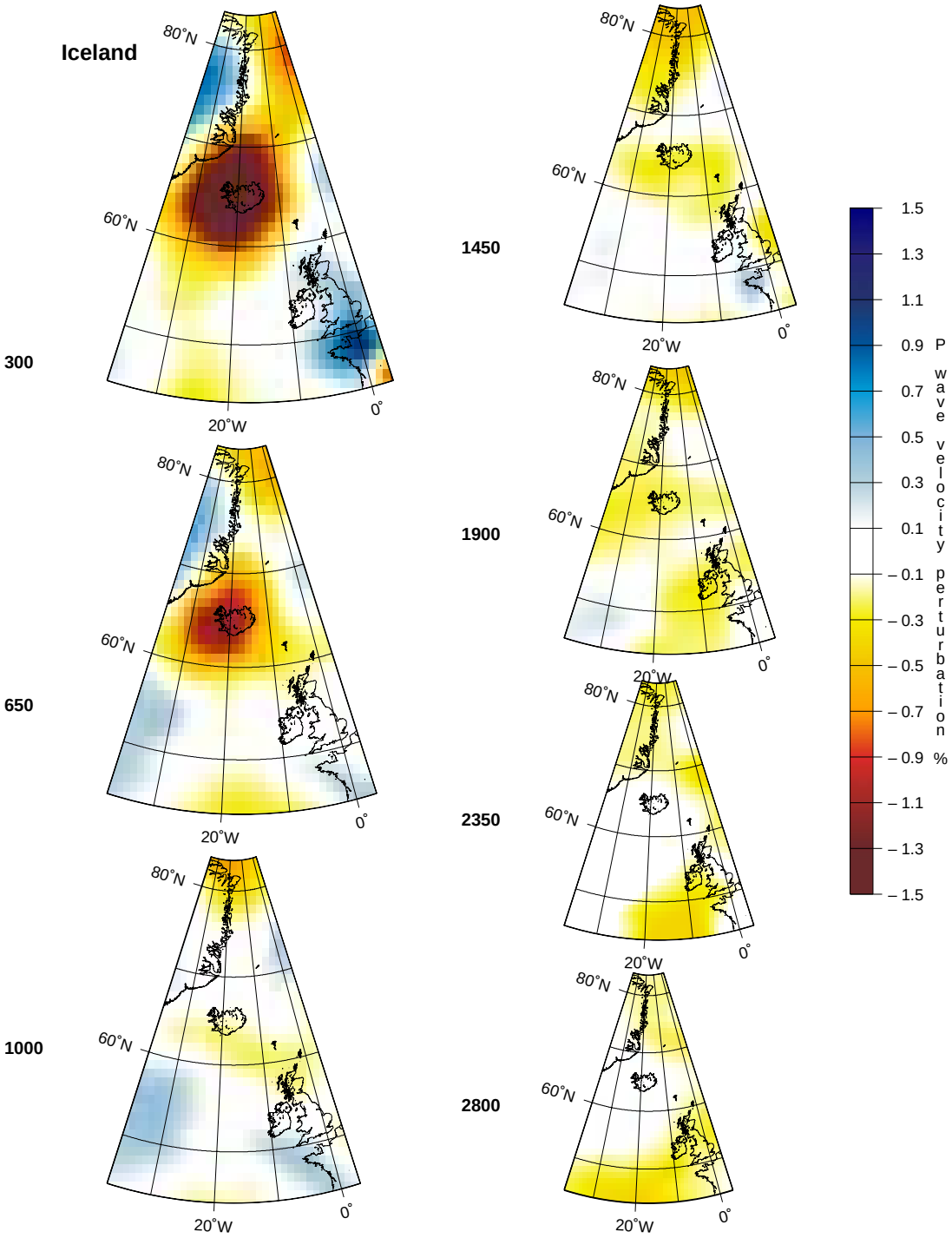

Figure S15: Sections of the velocity model beneath Iceland (Fig. 3). Plotting format is the same as in Fig. S2.

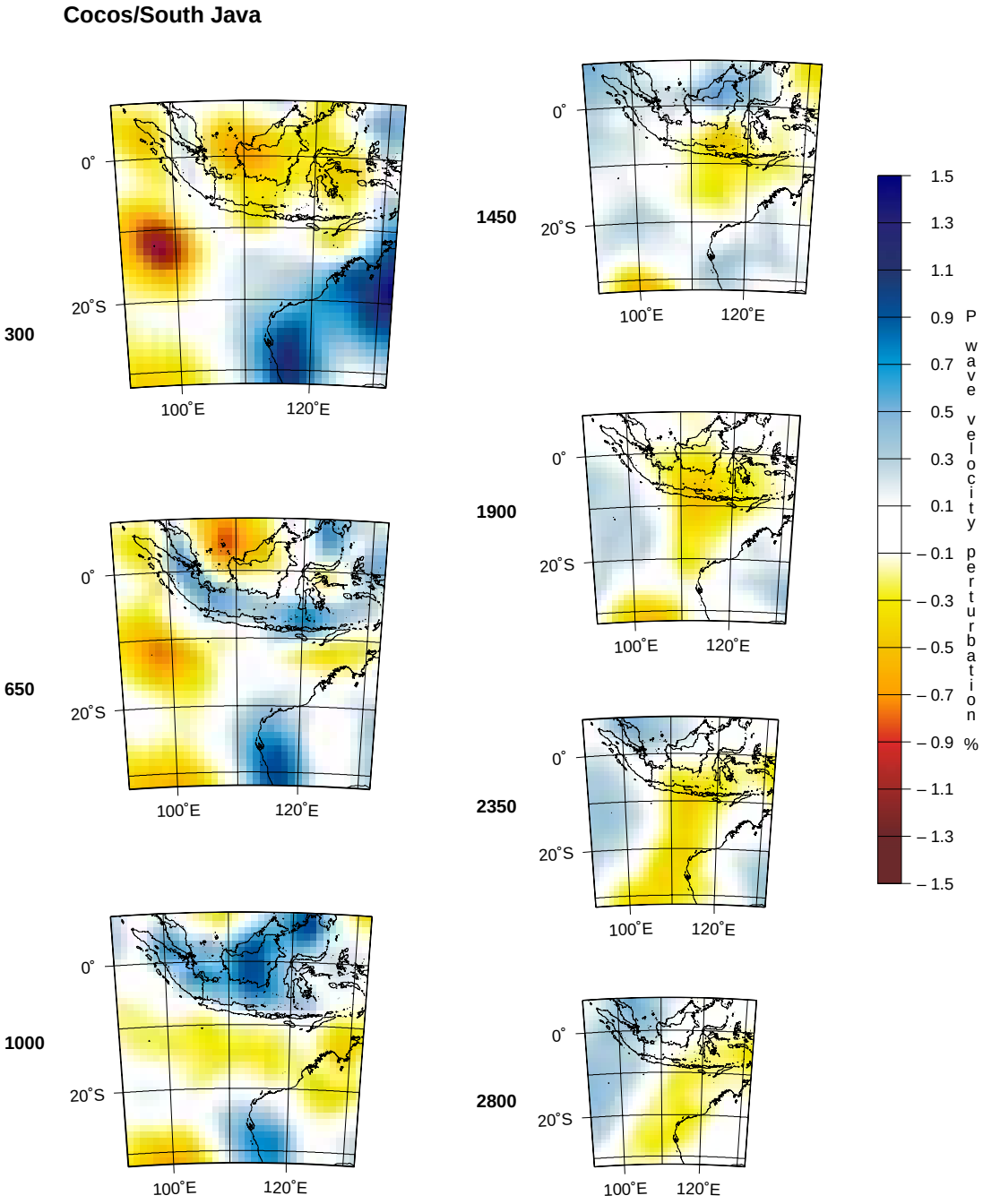

Figure S16: Sections of the velocity model beneath Cocos-Keeling and South of Java (Fig. 3). Plotting format is the same as in Fig. S2.

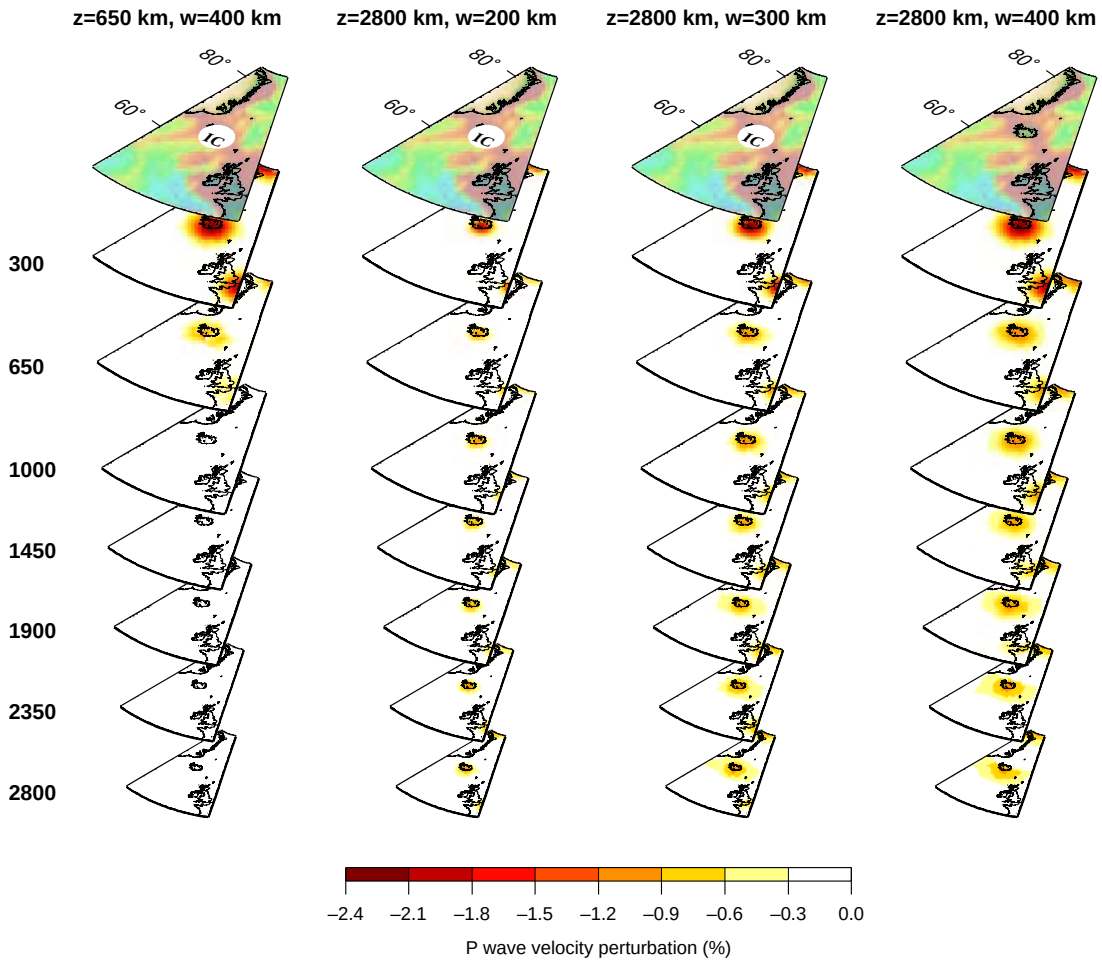

Figure S17: To estimate the width and depth reliability of the low-velocity anomalies found in the velocity model, we use different plume widths (radii of 100, 200, 300 and 400 km, respectively) for plumes originating at different depths in the mantle: 650, 1000, 1450, 1900, 2350 and 2800 km. The radial velocity perturbation in the synthetic plume is a three-dimensional Gaussian centered on the axis of the plume; the anomaly amplitude varies with depth in the manner predicted by Karato [5] for a temperature contrast of $\Delta T = 300$ K at the center. In this figure, we present three-dimensional views of the synthetic plumes used in the resolution tests of Figs. 2, 3 and S1–S16. Surface geography corresponds to the synthetic plumes beneath Iceland; plumes at other locations have the same geometry; z indicates the depth of the source region in km, and w is the radius in km. We only show the results obtained with plumes originating at 650 km depth with 400 km radius, and plumes originating at the bottom of the mantle with radii 200, 300 and 400 km, respectively. These resolution tests have been used to determine whether the shallow and mid-mantle plumes are the result of lack of resolution at depth and whether the mid-mantle and deep plume are due to leakage from the upper mantle.

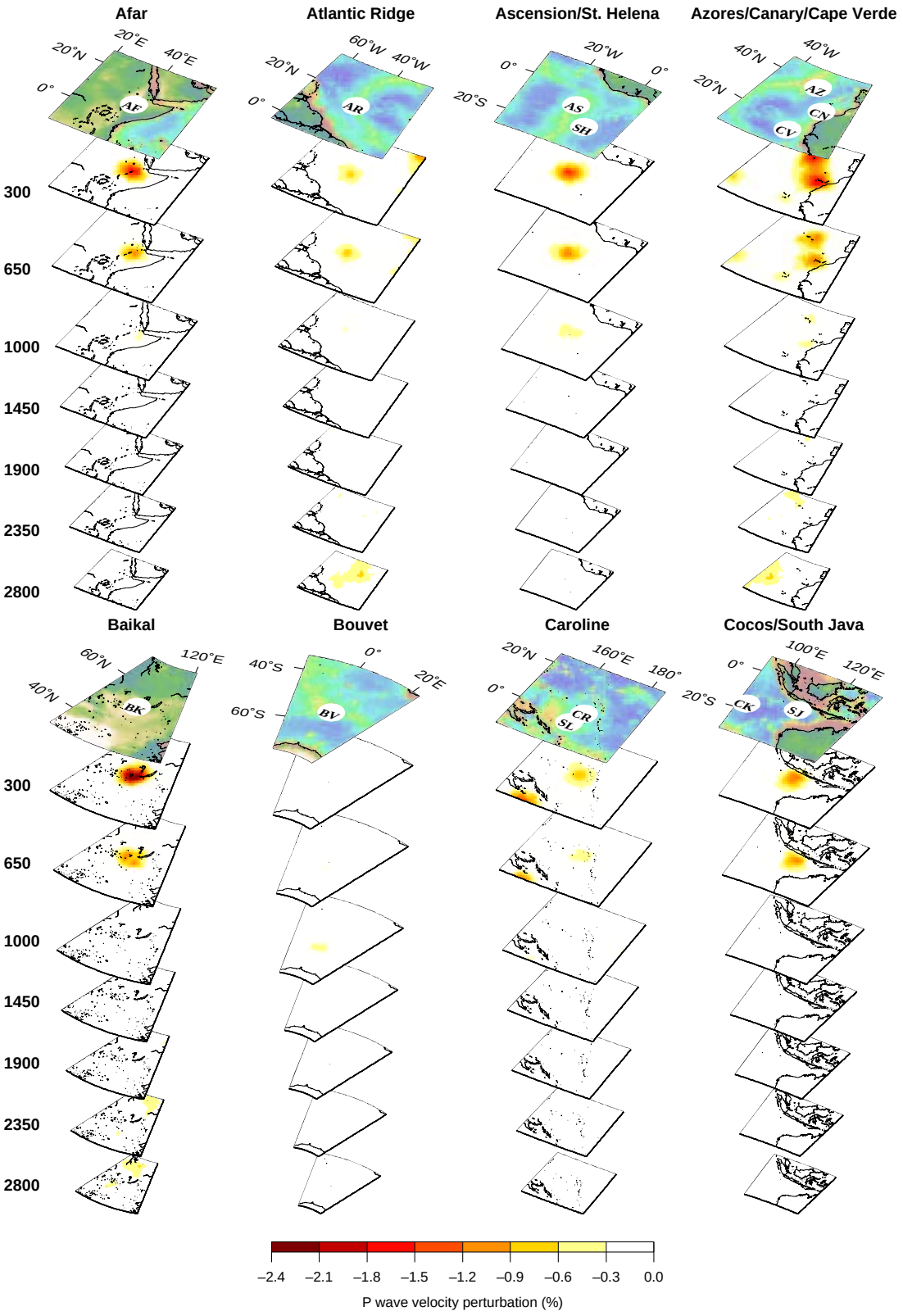

Figure S18: Reconstructed synthetic plumes whose input depth and radius are 650 km and 400 km, respectively. Plumes are listed alphabetically. Labels on the surface are listed in Table 1 and indicates published locations of the hotspots.

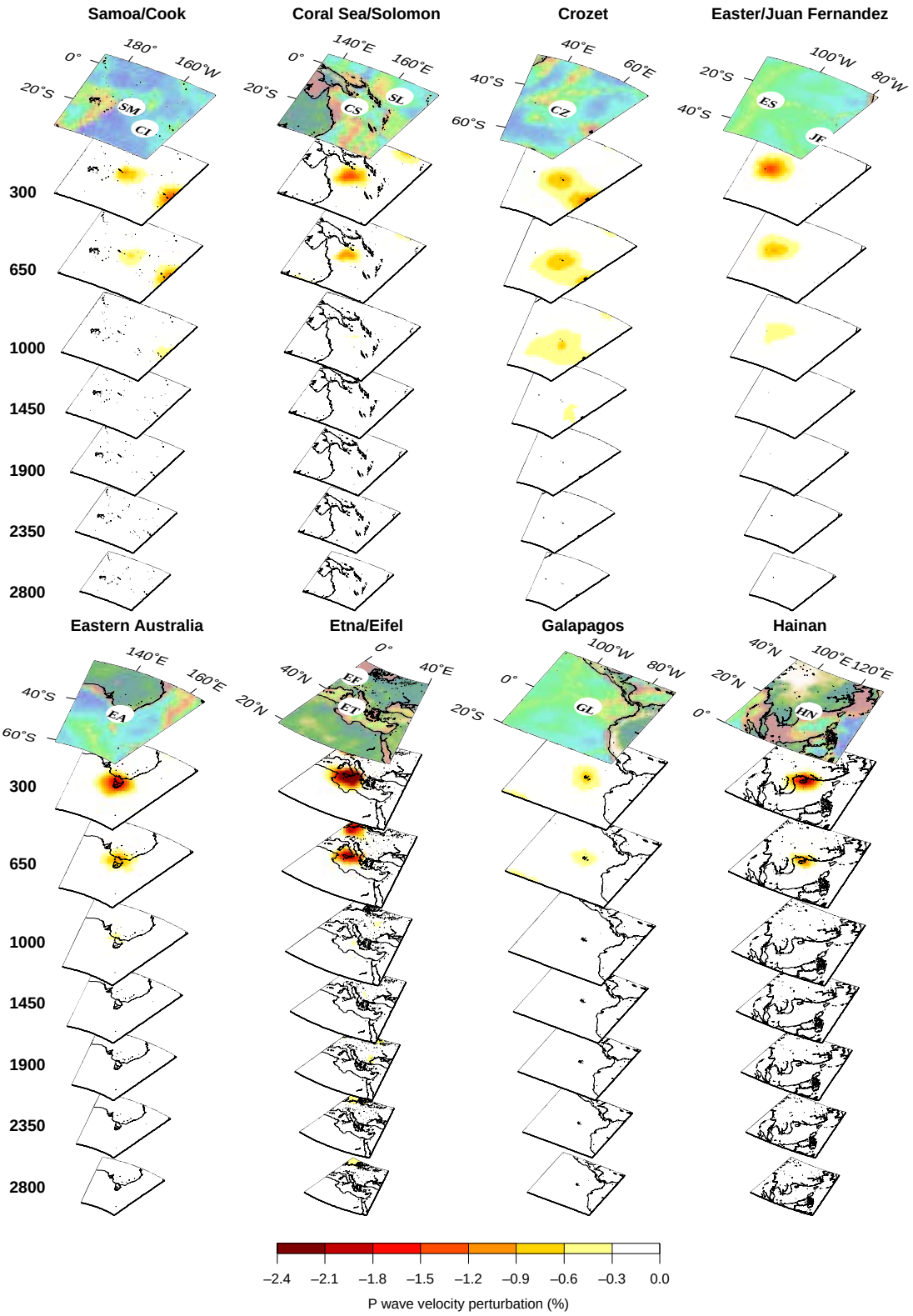

Figure S18 continue

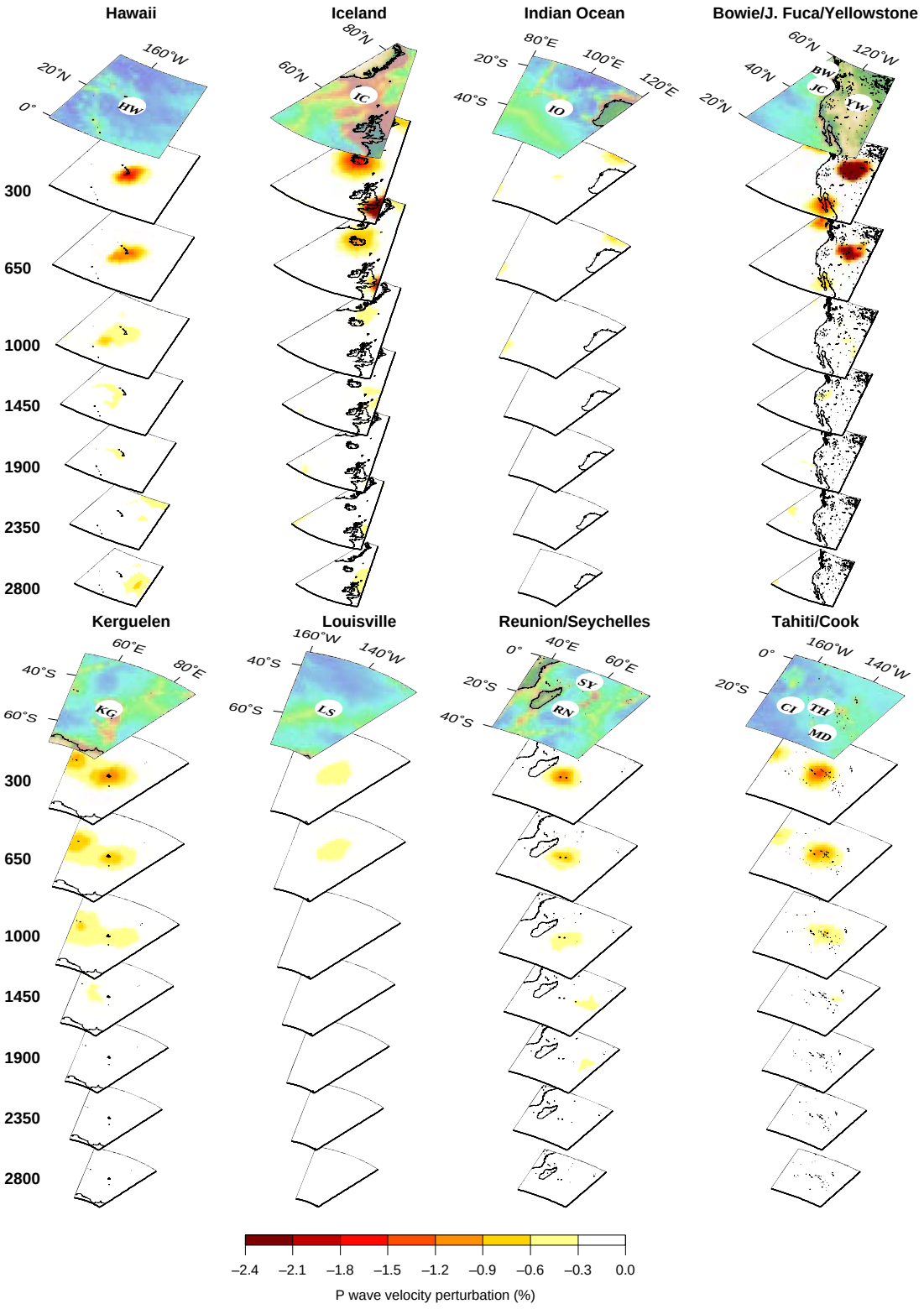

Figure S18 continue

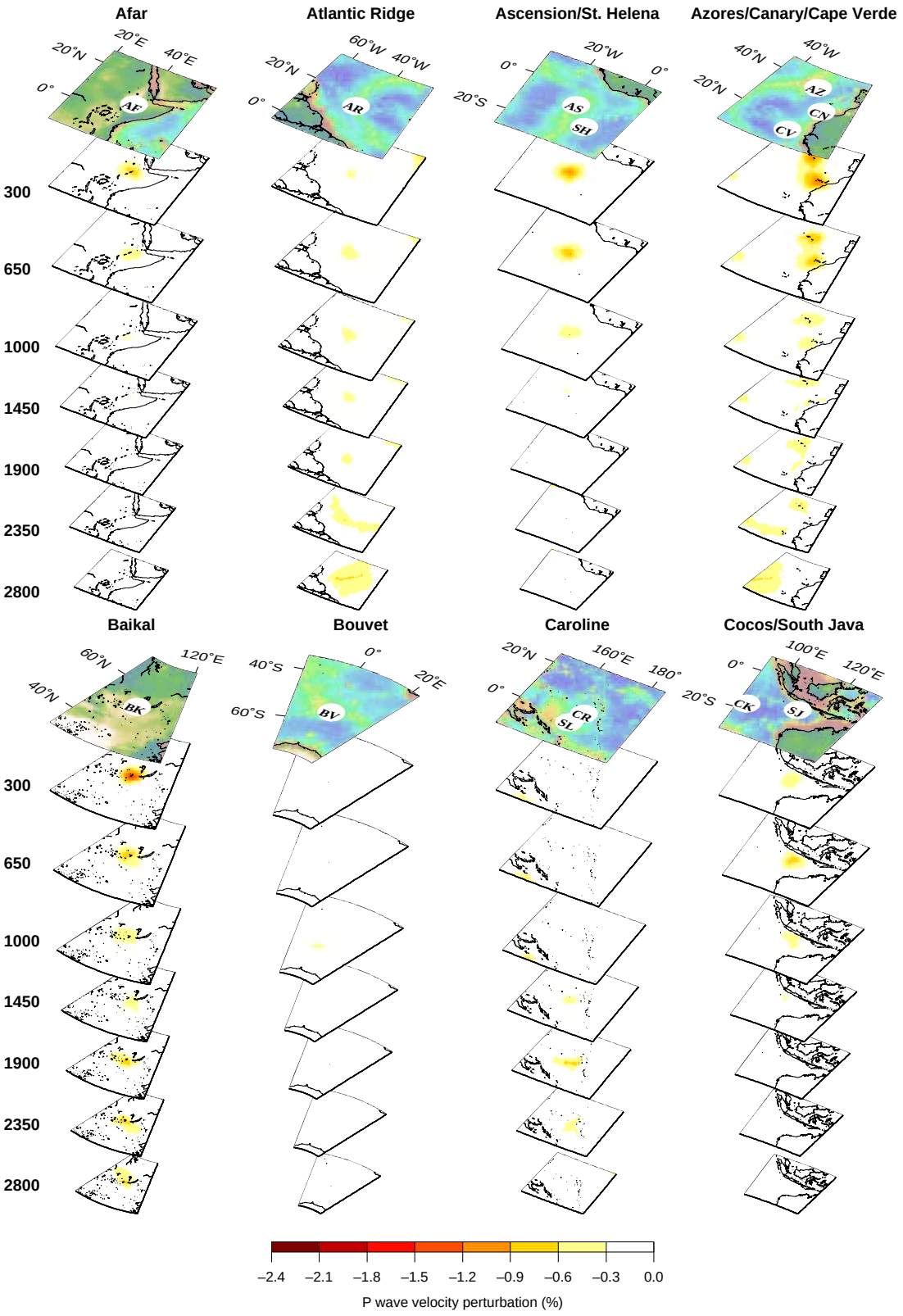

Figure S19: Reconstructed synthetic plumes whose input depth and radius were 2800 km and 200 km, respectively.

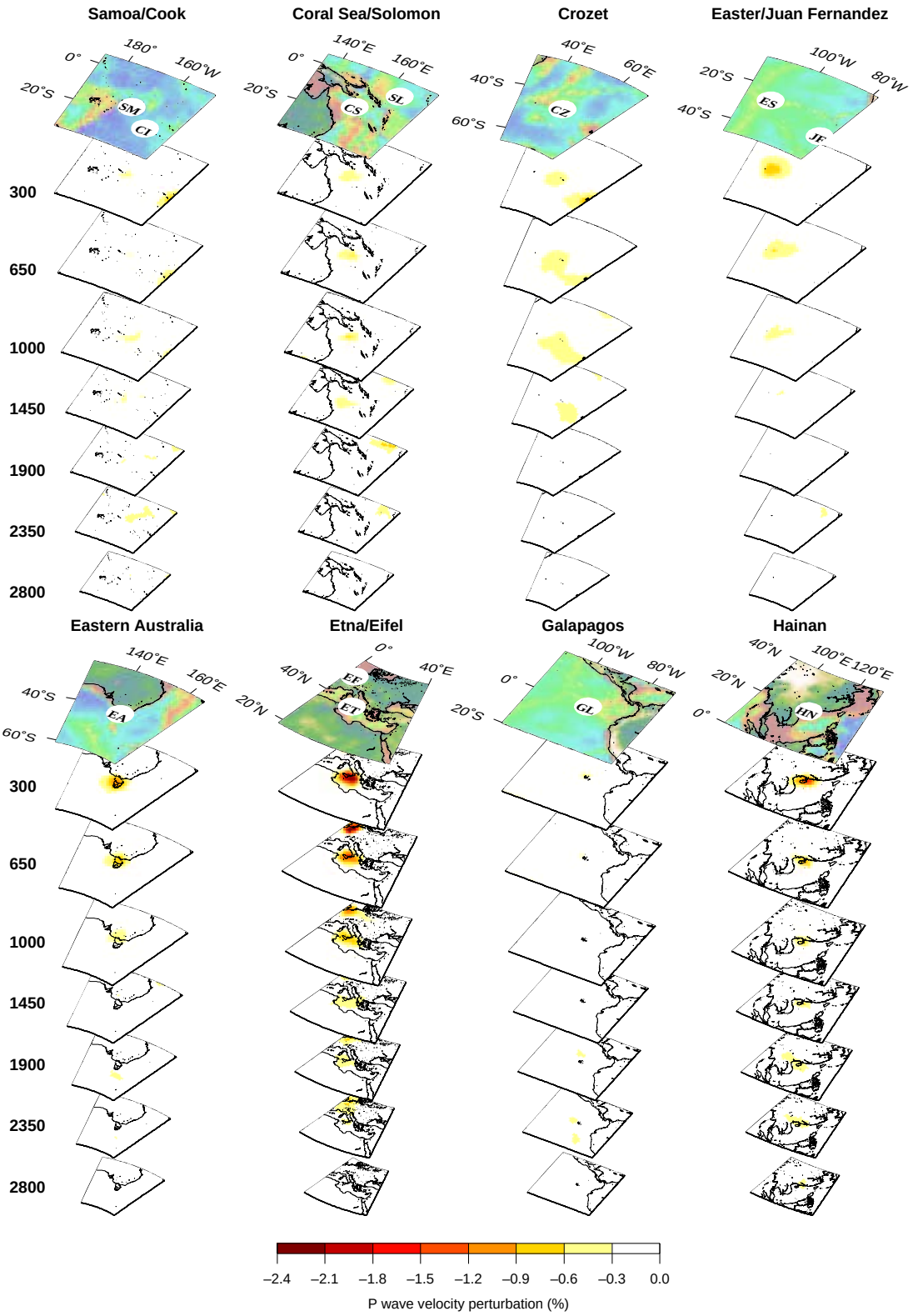

Figure S19 continue

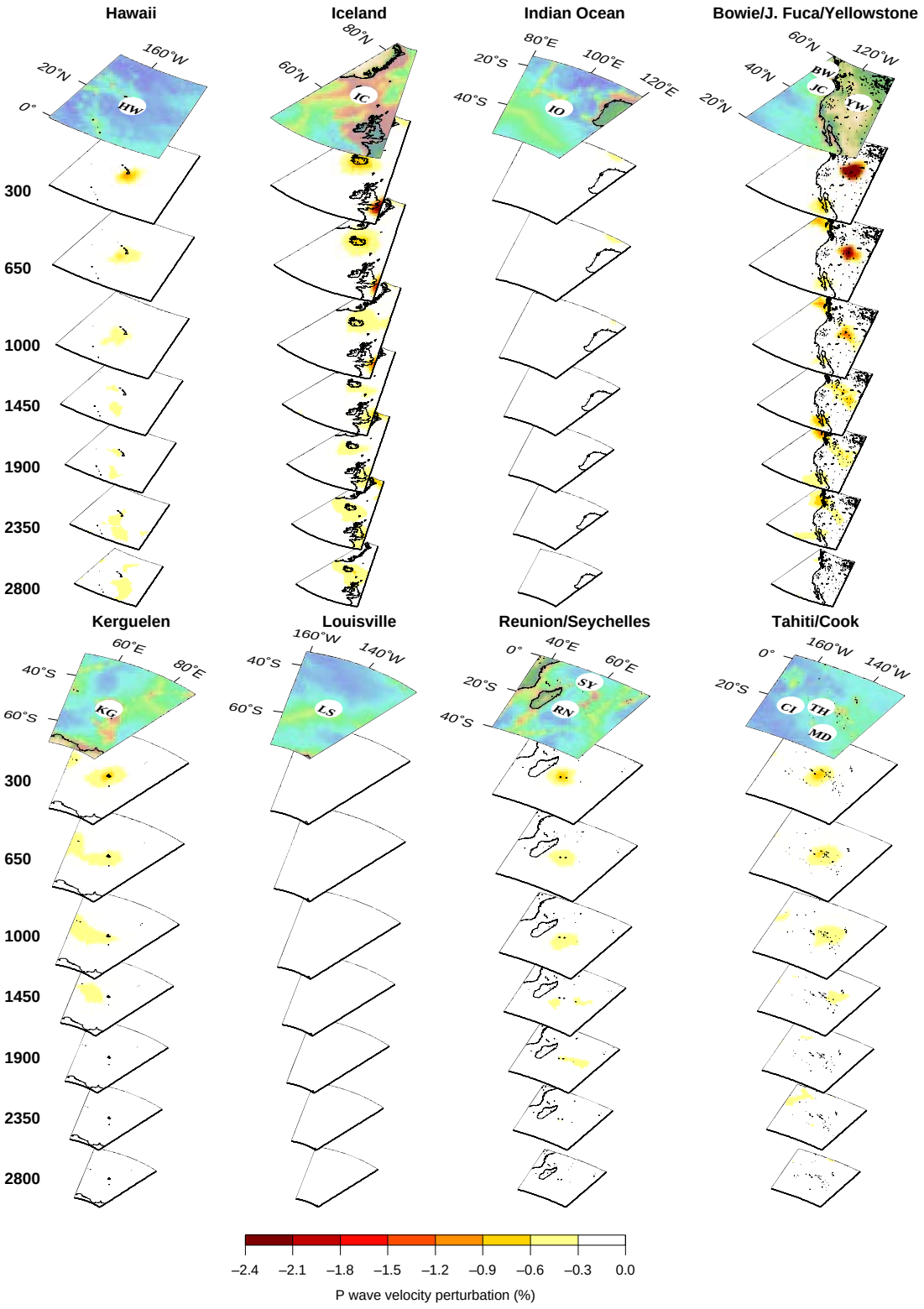

Figure S19 continue

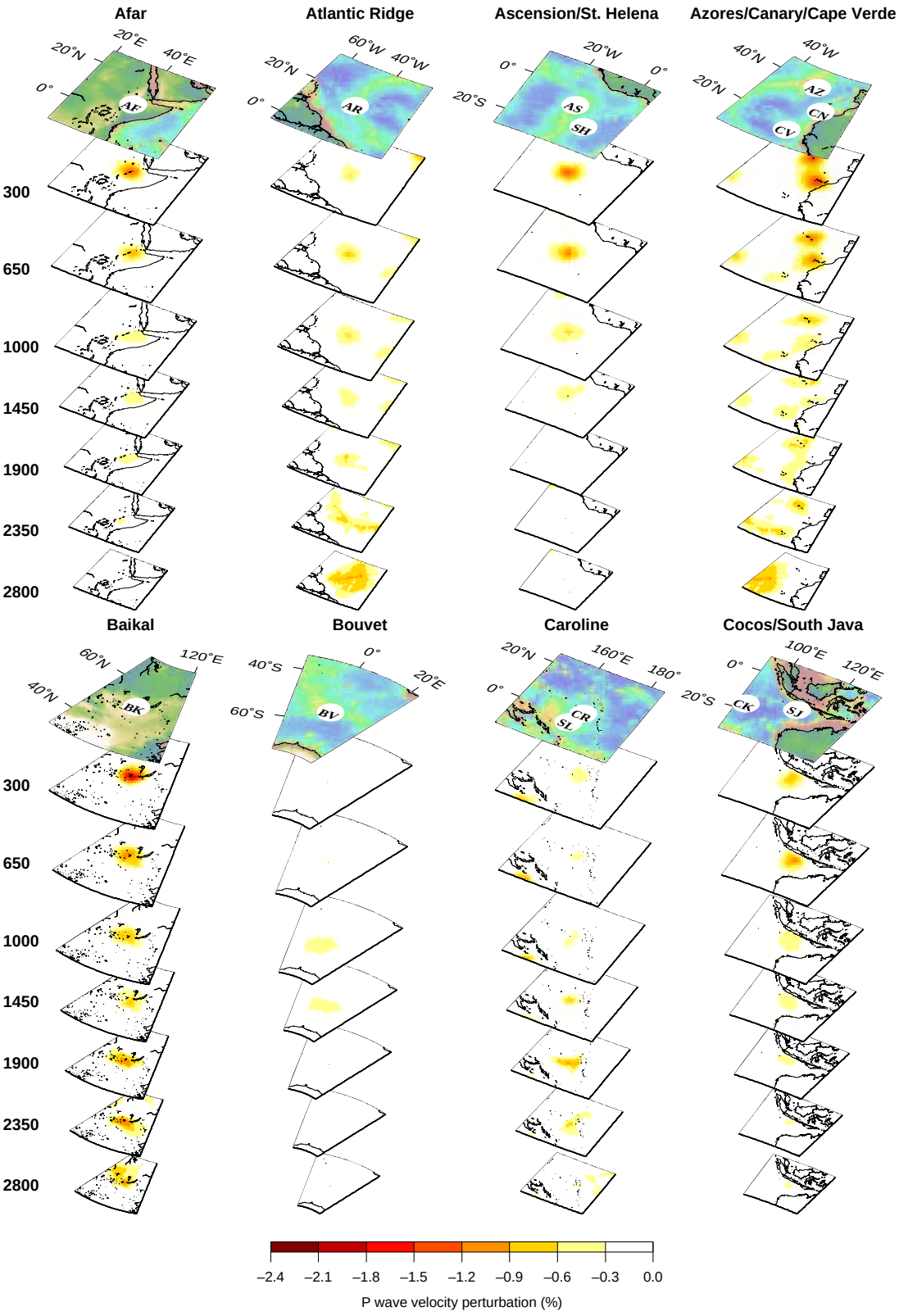

Figure S20: Same as Fig. S19, but for synthetic plumes with radius of 300 km.

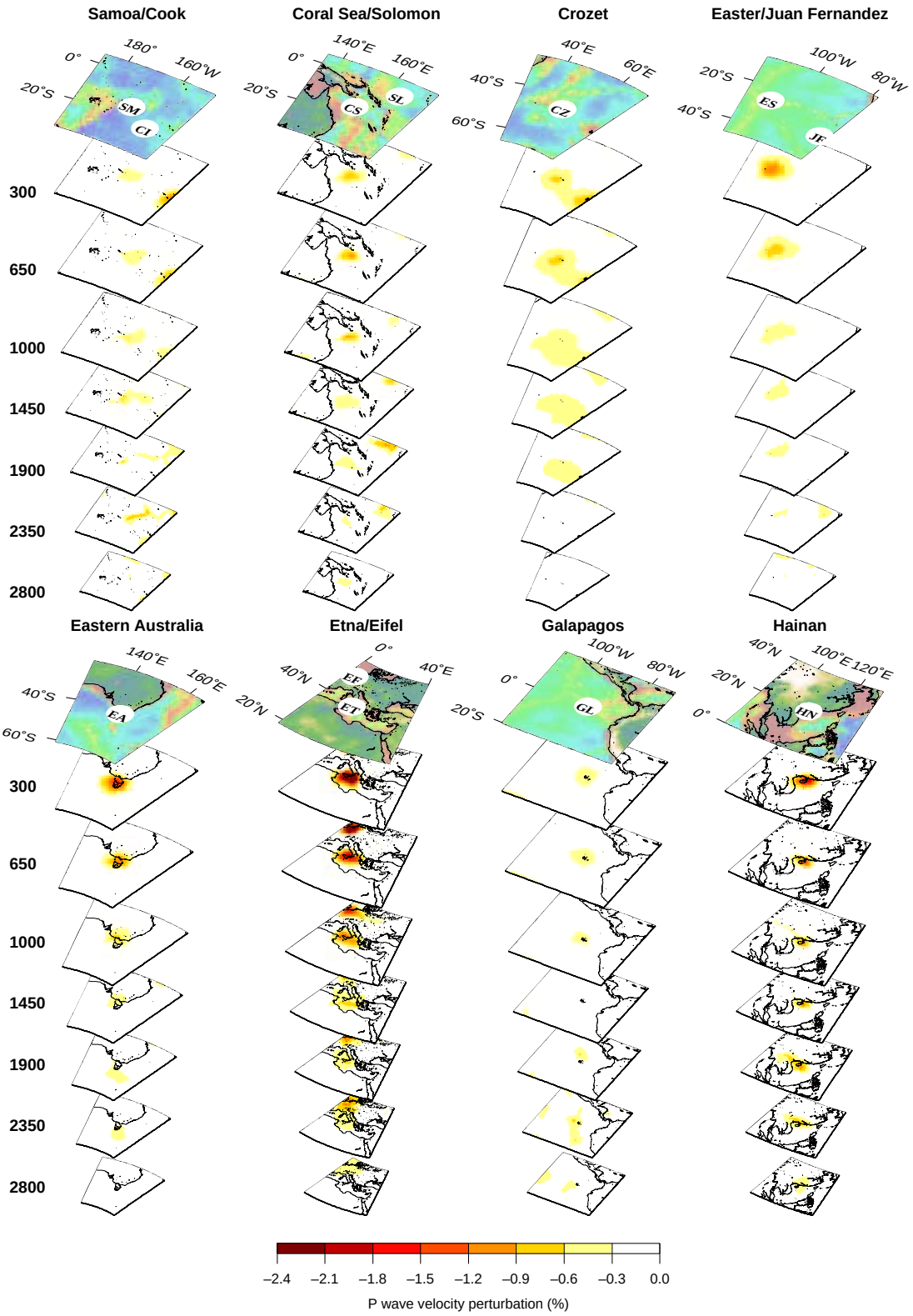

Figure S20 continue

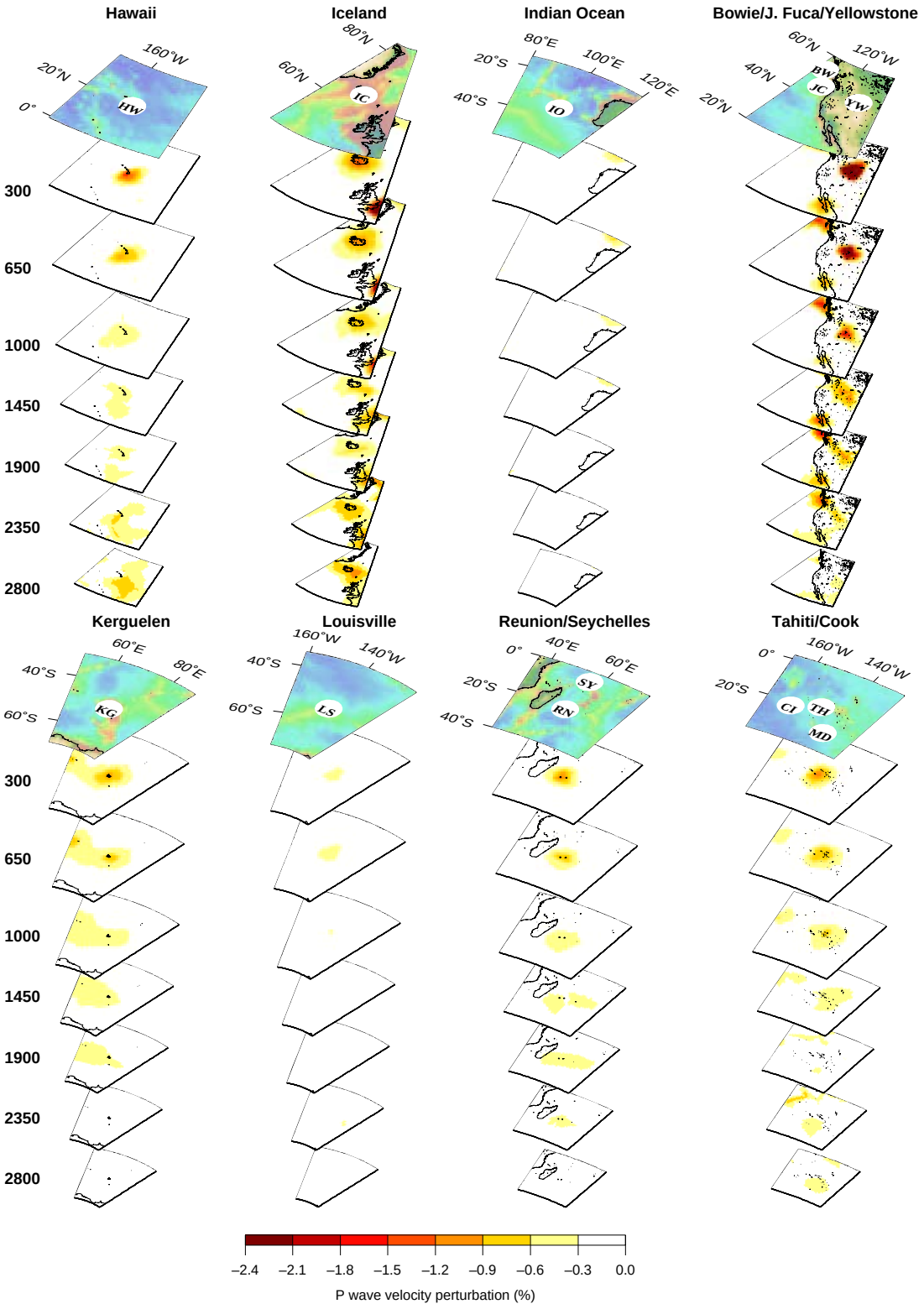

Figure S20 continue

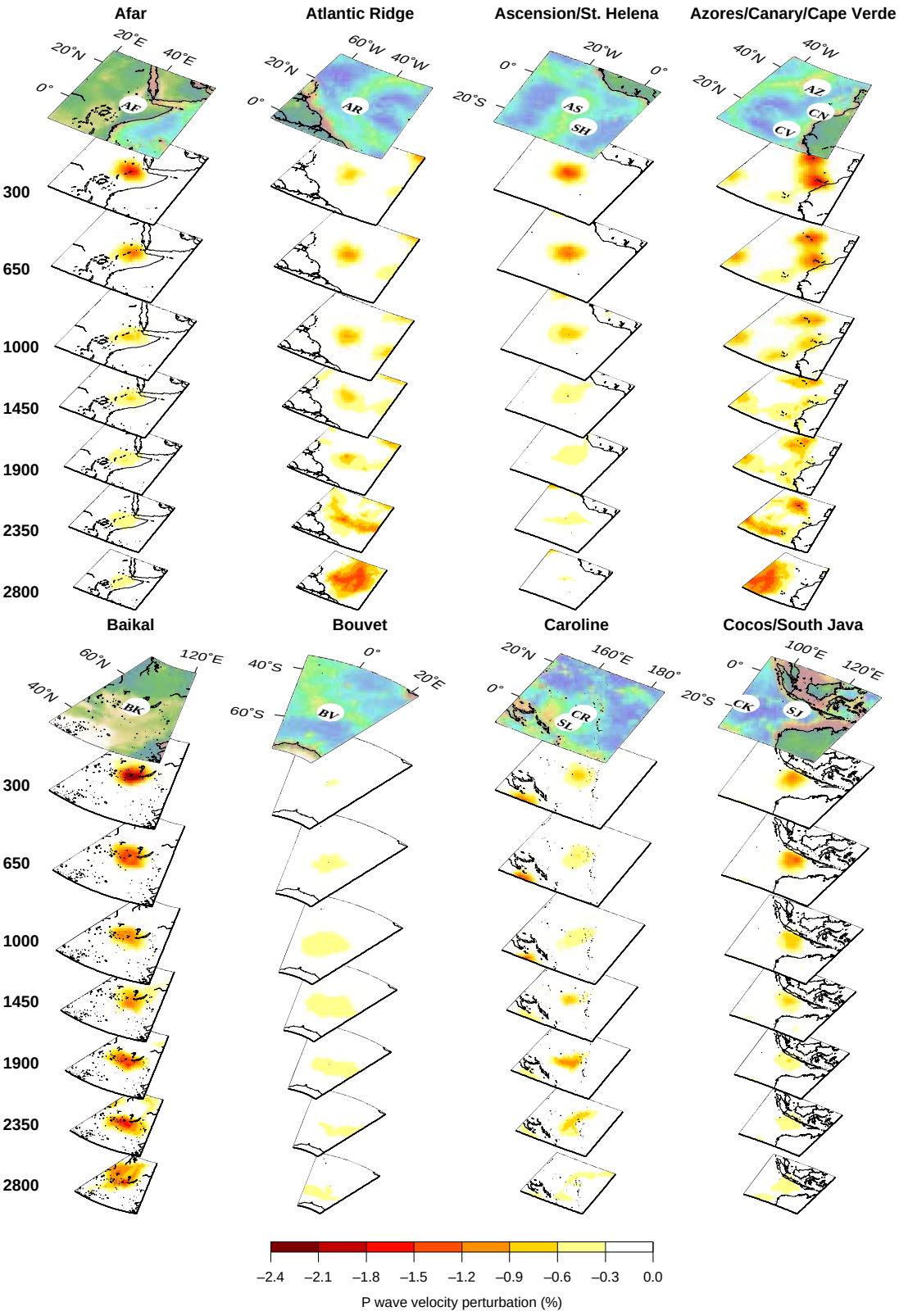

Figure S21: Same as Fig. S20 and S21, but for synthetic plumes with 400 km radius.

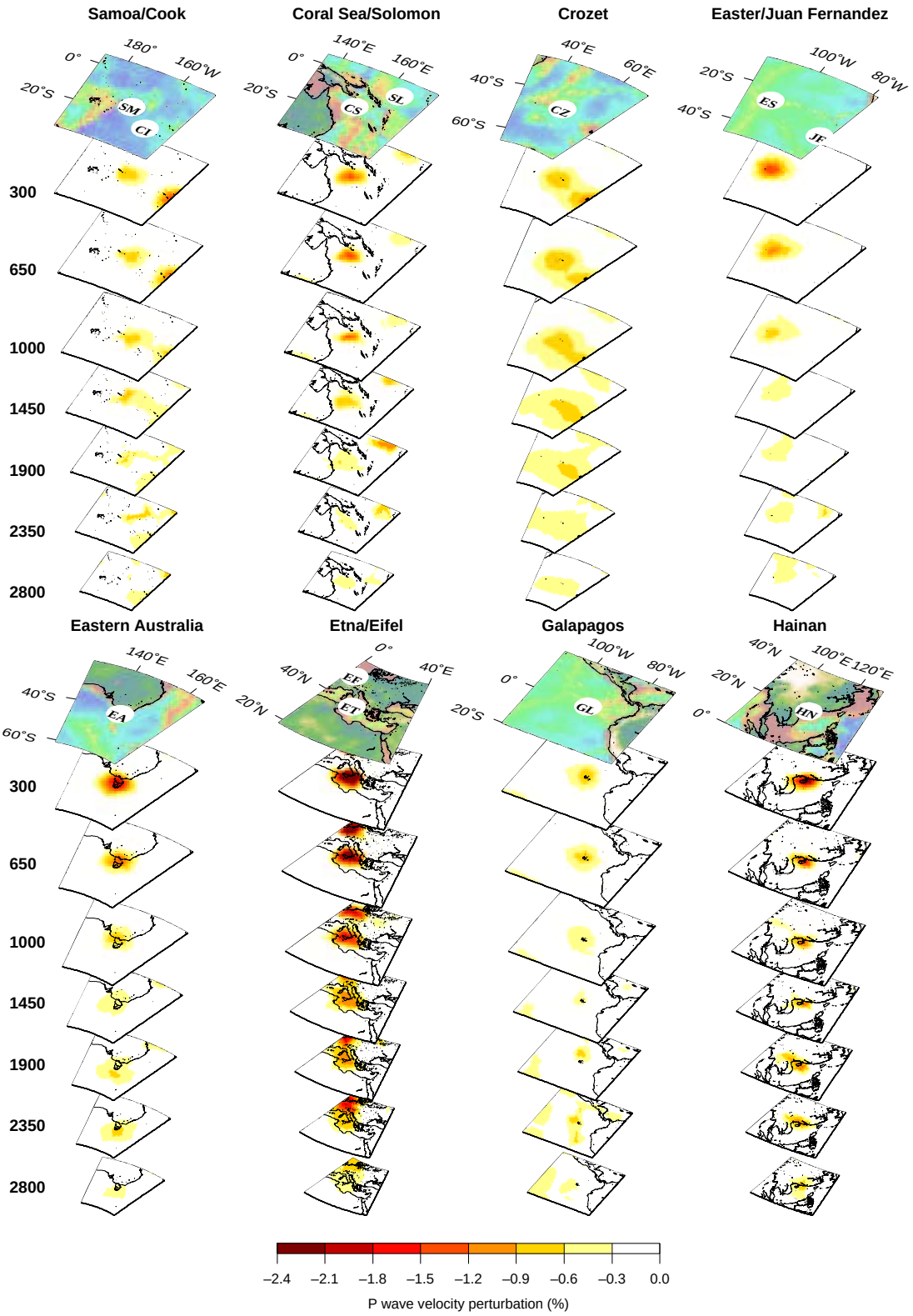

Figure S21 continue

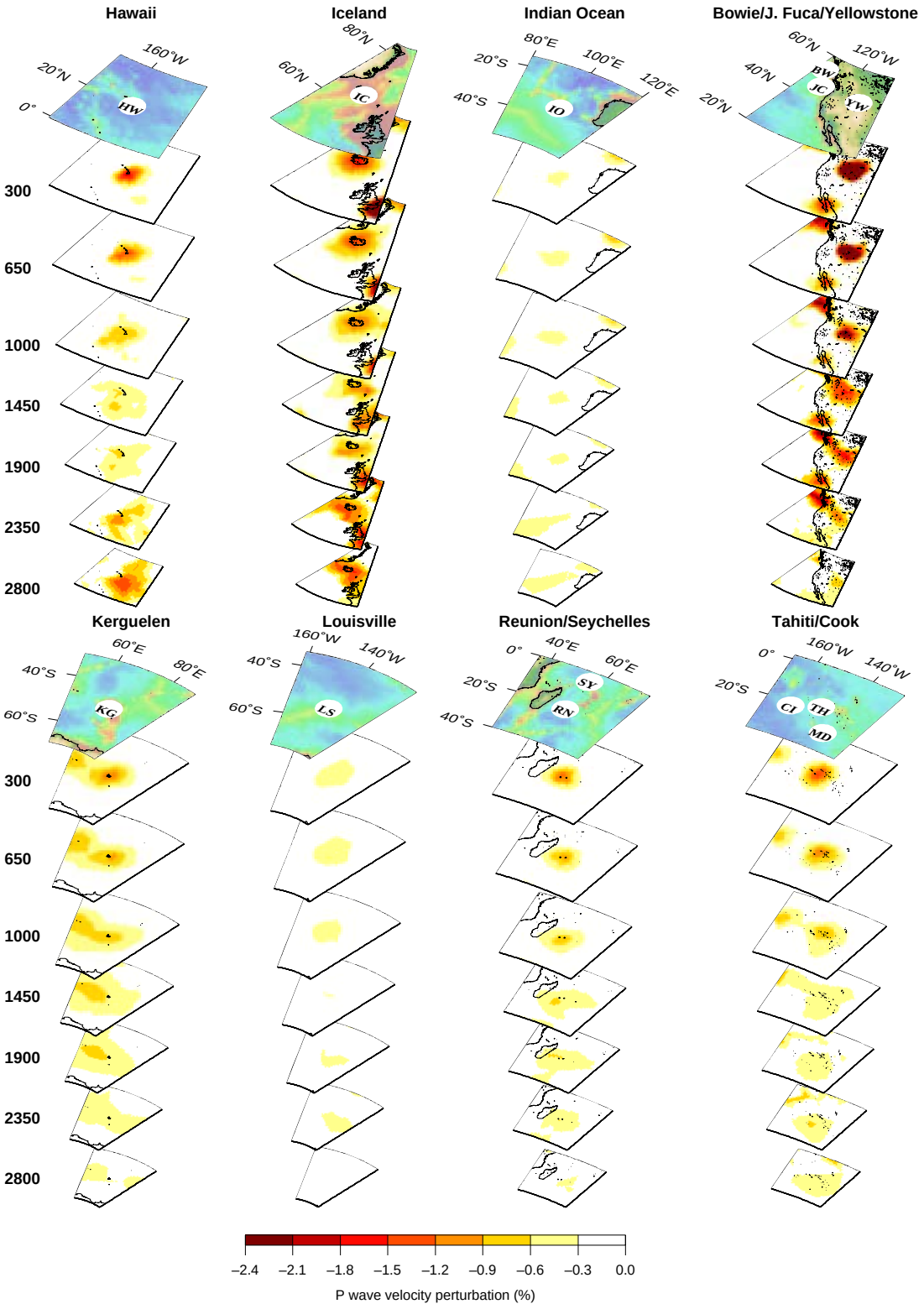

Figure S21 continue

References and Notes

[1] D. F. Watson, *Comput. J.* **24**, 167 (1981).

[2] D. F. Watson, *Contouring: A guide to the analysis and display of spatial data* (Pergamon, Oxford, 1992).

[3] M. Sambridge, J. Braun, H. McQueen, *Geophys. J. Int.* **122**, 837 (1995).

[4] G. Nolet, *Seismic Tomography*, G. Nolet, ed. (D. Reidel Publishing Company, 1987), pp. 1–23.

[5] S.-I. Karato, *Geophys. Res. Lett.* **20**, 1623 (1993).